Chapter 6

Adjoint tomography of the southern California crust

Note

This chapter is a draft of a paper to be submitted to *Geophysical Journal International*. Authors are Carl Tape, Qinya Liu, Alessia Maggi, and Jeroen Tromp. This research was the primary focus of my thesis from January 2007 to April 2009. Synthetics for the first updated model ($\mathbf{m}_{01}$) were computed in May 2008, and synthetics for the final model ($\mathbf{m}_{16}$) were computed February 2009. Key preceding studies by each coauthor are *Tape et al.* (2007), *Liu and Tromp* (2006), *Maggi et al.* (2009), and *Tromp et al.* (2005).

Summary

We iteratively improve a three-dimensional seismological model of the southern California crust using an inversion strategy based upon adjoint methods. The resulting model involved 16 tomographic iterations, which required 6800 wavefield simulations and a total of 0.8 million CPU-hours. The new crustal model reveals strong heterogeneity, including local changes of $\pm 30\%$ with respect to the initial 3D model provided by the Southern California Earthquake Center. The improved crustal model illuminates shallow features with a close correspondence to surface geology, such as sedimentary basins. It also reveals crustal features at depth that aid in the tectonic reconstruction of southern California, such as subduction-captured oceanic crustal fragments. The new model enables more realistic and accurate assessments of seismic hazard.

6.1 Introduction

The objective of seismic tomography is to produce detailed three-dimensional (3D) images of Earth's interior by minimizing the differences between simulated (or "synthetic") seismograms and recorded (or "observed") seismograms. Seismic tomography has been successful in producing images of Earth's interior, such as large-scale variations in the mantle (*Woodhouse and Dziewonski*, 1984; *Romanowicz*, 2003), subducting slabs (*Grand et al.*, 1997), and mantle plumes (*Montelli et al.*, 2004). These tomographic studies adopt a simple one-dimensional (layered) reference model (*Dziewonski and Anderson*, 1981), which allows for computationally inexpensive procedures within the minimization problem. Highly accurate numerical methods, such as the spectral-element method (SEM), may now be used to compute synthetic seismograms at regional and global scales, allowing tomographers to start the minimization procedure with more realistic 3D initial models and simulations (*Komatitsch et al.*, 2002; *Akçelik et al.*, 2003; *Chen et al.*, 2007; *Fichtner et al.*, 2009). Furthermore, as demonstrated in this study, these numerical methods may be exploited within the minimization problem by using so-called adjoint methods (*Tarantola*, 1984; *Talagrand and Courtier*, 1987; *Tromp et al.*, 2005).

Southern California provides an excellent motivation and setting for the two-fold objective of fitting seismograms and characterizing the crust. The station coverage (Figure 6.2a), especially in the Los Angeles region, is one of the densest in the world. A detailed 3D seismological model of the southern California crust has been constructed from a variety of seismic datasets (*Komatitsch et al.*, 2004). Several different approaches have been used to determine earthquake source parameters. Finally, an accurate wave propagation code, employing the SEM, has been applied to simulate seismic wave propagation in the region (*Komatitsch et al.*, 2004), with recent modifications to facilitate an inverse problem (*Liu and Tromp*, 2006).

"Adjoint tomography" involves the application of adjoint methods and 3D simulations of seismic wave propagation to seismic tomography (*Tromp et al.*, 2005; *Tape et al.*, 2007). The approach is that of a minimization problem: (1) specification of an initial model described in terms of a set of earthquake source parameters and 3D variations in density, shear-wave and bulk-sound speeds; (2) specification of a misfit function; (3) computation of the value of the misfit function for the initial model; (4) computation of the gradient (and Hessian,

if feasible) of the misfit function for the initial model; and (5) iterative minimization of the misfit function. This paper is organized following these steps, with emphasis on the new crustal model (Section 6.5).

Here we demonstrate the feasibility of our tomographic approach by iteratively improving a 3D crustal model of southern California. Within the iterative procedure we use traveltime measurements of body and surface waves from 52,000 three-component seismograms of 143 crustal earthquakes. After 16 iterations, the resulting crustal model generates seismic waveforms with substantially improved fits to observed waveforms and it captures features in the data that are not produced by the initial 3D model. The quality of the new crustal model allows us to simulate the details of earthquake ground motion at periods of two seconds and longer for hundreds of different paths in southern California. Our new crustal model contains strong vertical and lateral heterogeneity. Many new tomographic features are revealed, the most dramatic of which are the Coast Ranges and their numerous sedimentary basins, the southern San Joaquin basin, the mid-crust of the Mojave Desert region, and the mid-crust of the western Transverse Ranges.

6.2 Initial model

We compute synthetic seismograms using the spectral-element method (*Komatitsch et al.*, 2004). Due to the accuracy of the SEM, the goodness of fit between observed and synthetic seismograms depends only on the quality of the Earth structure model and the quality of the earthquake source model. Here we describe the structure and source parameters, followed by a description of the model vector $\mathbf{m}$ used in the tomographic inversion.

6.2.1 Initial 3D crustal model

We wish to use an initial seismological Earth model that produces the maximum number of measurements for a given set of earthquakes. Hence we begin with a 3D model (*Komatitsch et al.*, 2004) rather than a standard 1D layered model for southern California. The initial seismological model is provided by the Southern California Earthquake Center and contains results from several different seismic datasets: seismic reflection and industry well-log data to constrain the geometry and structure of major basins (*Süss and Shaw*, 2003; *Komatitsch et al.*, 2004; *Lovely et al.*, 2006), receiver function data to estimate the

depth to the Moho (*Zhu and Kanamori*, 2000), and local earthquake data to obtain the 3D background wavespeed structure (*Hauksson*, 2000; *Lin et al.*, 2007b). The seismological model is described in terms of shear wavespeed (V_S) and bulk sound speed (V_B), which can be combined to compute compressional wavespeed

$$V_P^2 = \tfrac{4}{3} V_S^2 + V_B^2 \; . \tag{6.1}$$

We extend the simulation region of *Komatitsch et al.* (2004) westward, so as to include the Coast Ranges (Figure 6.1). We also implement a more recent version of the background model (*Lin et al.*, 2007b), and we obtain density (ρ) by empirically scaling V_P (*Brocher*, 2005).

6.2.2 Earthquake sources

Each earthquake source is described by ten parameters: origin time (one), hypocenter (three), and moment tensor (six). Most of the epicenters and origin times were previously determined based upon the relocation technique of *Lin et al.* (2007a), and these remain unchanged during the iterative improvement of the seismological model. We perform numerous tests to determine the best focal mechanism for each earthquake, and we invert for the focal mechanisms (*Liu et al.*, 2004) once in the initial 3D model ($\mathbf{m}_{00}$) and again at the twelfth iteration ($\mathbf{m}_{12}$). The earthquake and station coverage for our study is shown in Figure 6.1.

Four criteria, in order of importance, influenced our selection of earthquakes for the tomographic inversion:

1. availability of quality seismic waveforms for the period range of interest (2–30 s) (must have at least 10 good stations);
2. availability of a relocated hypocenter (with origin time);
3. occurrence in a region with few other earthquakes;
4. availability of a "reasonable" initial focal mechanism.

These criteria led us to select earthquakes with $M_w \geq 3.4$, with the smallest ones in regions of sparse coverage. We represent the earthquakes as point sources in our simulations. Within

our period range of interest (2–30 s), this leads us to exclude earthquakes with $M_w > 5.5$. Because the computational cost of our technique is independent of the number of stations, we prefer to use larger earthquakes ($M_w \geq 4$). Larger earthquakes produce higher signal-to-noise ratios at more stations, thereby leading to more measurement windows.

We use the variable σ_0 to indicate the "water-level" minimum uncertainty associated with a traveltime measurement. For our tomographic inversion, we choose

$$\sigma_0 = 1.0 \text{ s} \tag{6.2}$$

based on the estimated uncertainties of earthquake source parameters. The tomographic inversion concentrates on reducing time shifts between synthetic and recorded waveforms that exceeded σ_0.

Epicenters

Earthquake epicenters are primarily from *Lin et al.* (2007a), where available. We supplement these with results from other local studies that used local and temporary stations. These local studies include *Lohman and McGuire* (2007) for a swarm of earthquakes in the Salton trough, *Thurber et al.* (2006) for earthquakes in the Parkfield region, and *McLaren et al.* (2008) for earthquakes in the San Simeon region. These studies all employed the double-difference method of *Waldhauser and Ellsworth* (2000), and generally provide the hypocenters and origin times of earthquakes, as well as a 3D tomographic model.

Epicenters—the latitudes and longitudes of the earthquakes—are the best determined source parameters. The seismicity studies listed above used a much larger dataset of traveltime picks to locate the earthquakes than we do in the tomographic inversion. The majority of the epicenters are from *Lin et al.* (2007a,b), who used P and S arrival times from 783 stations, including strong motion stations and temporary arrays. The dense coverage of stations in the vicinity of the earthquakes (e.g., the Parkfield array used in *Thurber et al.*, 2006) is important for epicenter estimation, as well as for depth and origin time. *Lin et al.* (2007a,b) also used information from controlled sources (quarry blasts and shots) to estimate uncertainties of absolute locations and absolute origin times (*Lin et al.*, 2006). The changes in wavespeed produced by our tomographic inversion are large (±30% locally) but

they impart only minor traveltime shifts[1] compared to $\sigma_0 = 1.0$ s. Therefore, we do not change the epicenters during the iterative tomographic inversion.

Depths and origin times

Our initial depths and origin times are from the relocated catalogs in Section 6.2.2, where available. If relocated source parameters are not available, then we use the source parameters listed in the Southern California Earthquake Data Center catalog. At model iteration $\mathbf{m}_{12}$, we performed source inversions that allowed the depths to change (Section 6.2.2), and we also applied an empirical correction to the origin times (discussed next). These adjustments to the depths and origin times induced time shifts much smaller than $\sigma_0 = 1.0$ s.

We noticed a minor, magnitude-dependent time-shift pattern, based on analysis of near-source seismograms for model $\mathbf{m}_{12}$ for the period range 2–30 s. The pattern indicated that larger events had systematically positive time shifts, even for stations in the vicinity of the earthquake source. We therefore modified the origin times of the sources with an empirical relationship given by $t_s = t'_s + 0.5h$, where t'_s is the listed origin time, h is the half-duration of the source (determined directly from M_{w}), and t_s is the new origin time. (t_s and t'_s are in "absolute" seconds, that is, with a particular reference zero-time; h is in seconds.) The maximum correction factor $0.5h$ for all 234 earthquakes was 0.65 s, the minimum was 0.06 s, the mean was 0.14 s, and the median was 0.11 s. Thus, all correction factors were less than $\sigma_0 = 1.0$ s. This minor adjustment in origin time is due to the fact that the origin time is derived from P wave picks on the unfiltered seismograms (thus, highest frequency) (*Allen*, 1978), while the origin time in our simulation is taken to be the *center* of a Gaussian source-time function with half duration h.

Focal mechanisms

Our initial focal mechanisms are selected from published catalogs of *Tan* (2006), *Hardebeck and Shearer* (2003), and the Southern California Earthquake Data Center (*Clinton et al.*, 2006). *Tan* (2006) implemented the "cut-and-paste" method (*Zhao and Helmberger*, 1994; *Zhu and Helmberger*, 1996), which uses both surface waves and body waves. The method of

[1] We illustrate this with an extreme example, considering an earthquake at $z = 10$ km depth, overlain by a region of $v_1 = 3$ km/s in the initial model, and we then apply a (very large) $n = \ln(v_1/v_2) = -0.3$ change in wavespeed. For a station immediately above the earthquake, the change in traveltime due to the change in structure will be $\Delta t = (z/v_1)[\exp(-n) - 1] \approx 1.2$ s. Thus, this extreme scenario produces a time shift slightly larger than $\sigma_0 = 1.0$ s.

Hardebeck and Shearer (2003) uses amplitude ratios between P and S waves. *Clinton et al.* (2006) implemented the method of *Pasyanos et al.* (1996) and *Dreger et al.* (1998), which uses relatively long-period surface waves (10–50 s). In cases where there were significant discrepancies among the mechanisms reported by different studies, we performed 3D simulations and compared the synthetics directly with the data to determine the best starting mechanism for the SEM-based inversion, discussed next.

Earthquake source inversions using 3D models

We performed inversions for earthquake focal mechanisms (*Liu et al.*, 2004) twice using the 3D crustal models: once at $\mathbf{m}_{00}$ and again at $\mathbf{m}_{12}$. For the inversion at $\mathbf{m}_{00}$, we inverted for the focal mechanism only, while keeping the hypocenter and origin time fixed. For some earthquakes, such as those near the Salton trough, the Ventura basin, and offshore Continental Borderlands, the quality of the inverted mechanism was affected by the poor quality of the initial source.

For the inversion at $\mathbf{m}_{12}$, we performed an SEM inversion first in the routine manner (*Liu et al.*, 2004), which starts with an initial focal mechanism. We also performed a (new) global grid search inversion that does not use the initial focal mechanism at all. Equipped with a much improved 3D crustal model ($\mathbf{m}_{12}$), we allowed both the focal mechanism and depth to change, while keeping the epicenter and origin time fixed. The mean and median depth changes for all earthquakes were both less than 0.5 km. We did not adjust the origin times based on changes to the depths, primarily because the changes in depth induced a traveltime shift[2] that was generally much less than $\sigma_0 = 1.0$ s.

6.2.3 Model variables, model parameterization, and model vector

We are therefore faced with constructing a model vector $\mathbf{m}$ for the tomographic inversion. The elements of $\mathbf{m}$ must describe the two continuous scalar fields $V_{\mathrm{S}}(\mathbf{x})$ and $V_{\mathrm{B}}(\mathbf{x})$, where $\mathbf{x}$ is a point in the volume. The continuous fields are represented using basis functions, which we choose to be the same ones used in solving the forward problem numerically (*Tape et al.*, 2007). Thus, each (local) gridpoint in the numerical mesh, $\mathbf{x}_i$, has a corresponding value

[2]To illustrate this point, consider the extreme example of an earthquake at depth z with a station directly above it. The change in traveltime due to a change in earthquake depth is $\Delta t = \Delta z / v$. In order to match $\sigma_0 = 1.0$ s, at which point we would consider modifying the origin time, we would need a 1 km depth change (larger than what we generally applied) beneath a layer with a wavespeed of 1 km/s, which is much slower than the (2–30 s) wavespeed structure in most earthquake source regions.

of V_S and V_B that appear as elements of the model vector $\mathbf{m}$. The model vector has $2G$ elements, with G the number of (local) gridpoints in the mesh, and 2 the number of inversion variables (V_S and V_B). We use a subscript to denote the model iterations, such that $\mathbf{m}_{00}$ is out initial model, and $\mathbf{m}_{16}$ is our final model.

6.3 Misfit function

6.3.1 Selection of bandpasses

The quality of fit between observed and synthetic seismograms is strongly dependent on the frequency content of the seismic waves, because the overall quality of the model generally diminishes with shortening scalelength. We therefore examine multiple period ranges: 6–30 s, 3–30 s, and 2–30 s. Our choice emphasizes fitting seismic waveforms in the period range 6–30 s, which, for crustal earthquakes in southern California, is dominated by surface waves. Table 6.4 summarizes measurements for the final tomographic model.

6.3.2 Selection of time windows

Because our synthetic seismograms are computed using a complex 3D seismological model, we require a measurement tool that can capture the complex effects of wave propagation. We use an automated algorithm (*Maggi et al.*, 2009) to select time windows for the entire seismic dataset. A given time window, or "measurement window," is selected if there is a user-specified, quantifiable level of agreement between the observed and simulated seismograms.

We use an automated algorithm, FLEXWIN, for picking seismogram time windows that contain a quantifiable level of agreement between synthetics and data (*Maggi et al.*, 2009). The algorithm requires several user parameters that need to be adjusted for a given dataset (Table 6.2). The only differences between our values and those listed in *Maggi et al.* (2009, Table 3) are for the quantities that specify the maximum allowable time shifts between data and synthetics: $\Delta\tau_0$ and $\Delta\tau_{\text{ref}}$. The values in *Maggi et al.* (2009) are based on the $\mathbf{m}_{00}$ synthetics, which contain time shifts in excess of 10 s, comparable to what is shown in Figure 6.3b. However, using $\mathbf{m}_{16}$, there are no identifiable time shifts larger than 5 s, and the standard deviation of the time shifts is less than 1 s. Thus, with $\mathbf{m}_{16}$ we specify FLEXWIN parameters to only allow windows to be considered in which the absolute value

of the time shift is less than 4 s (6–30 s records), 3 s (3–30 s records), and 2 s (2–30 s records) (Table 6.2).

As our crustal model improved, we began to notice agreement between data and synthetics for time intervals *after* the expected surface-wave arrival times. We therefore modified the user functions stated in *Maggi et al.* (2009, Section A1.3), by *not* raising the water-level at the end-time of the expected surface wave.

Although the window-picking algorithm is automated, it is important to examine every single time window for the period ranges 6–30 s and 3–30 s. By carefully examining all the window picks at each iteration, we were able to lower the window acceptance criteria, thereby allowing more windows to be selected. This led to the automated selection of additional windows that needed to be manually excluded. If computation is unlimited, then one could instead raise the acceptance criteria to the point where very little hand-checking of the windows is needed, although fewer windows are then used in the in the tomographic inversion.

6.3.3 Misfit measures

We consider two measures of misfit: a traveltime difference (F_{t}) and a waveform difference (F_{w}). We use the traveltime misfit measure within the tomographic inversion, such as the generic equations in Equations (6.5) and (6.6). We use the waveform misfit measure to assess the misfit reduction, because in many cases there is a waveform in the $\mathbf{m}_{16}$ synthetics to align with the data, but there is no corresponding waveform in the $\mathbf{m}_{00}$ synthetics (e.g., Figure 6.3b, 6.4b).

For a single time window on a single seismogram, the traveltime and waveform misfit measures are given by

$$F_{\mathrm{t}}(\mathbf{m}) = \int_{-\infty}^{\infty} \frac{h(\omega)}{H} \left[\frac{\Delta T(\omega, \mathbf{m})}{\sigma_{\mathrm{t}}}\right]^2 \mathrm{d}\omega \,, \tag{6.3}$$

$$F_{\mathrm{w}}(\mathbf{m}) = \frac{\displaystyle\int_{-\infty}^{\infty} w(t) \left[d(t) - s(t, \mathbf{m})\right]^2 \mathrm{d}t}{\left(\displaystyle\int_{-\infty}^{\infty} w(t) \left[d(t)\right]^2 \mathrm{d}t \int_{-\infty}^{\infty} w(t) \left[s(t)\right]^2 \mathrm{d}t\right)^{1/2}} \,, \tag{6.4}$$

where $d(t)$ denotes the recorded time series, $s(t, \mathbf{m})$ the simulated time series, $\sigma_{\mathrm{t}} \geq \sigma_0$ the estimated uncertainty associated with the traveltime measurement, $w(t)$ a time-domain

window, and $h(\omega)$ a frequency-domain window with associated normalization constant $H = \int_{-\infty}^{\infty} h(\omega)\mathrm{d}\omega$. The frequency-dependent traveltime measurement, $\Delta T(\omega, \mathbf{m})$, is made using a multitaper method (e.g., *Laske and Masters*, 1996; *Zhou et al.*, 2004). In the case of a frequency independent measurement, $\Delta T(\omega, \mathbf{m})$ reduces to a cross-correlation traveltime measurement. The expression for F_{w} (Eq. 6.4) contains the same normalization as the standard cross-correlation formula and has been used for source inversions (*Zhu and Helmberger*, 1996, Eq. 3).

6.3.4 Misfit function

In the tomographic inversion, within each measurement window we choose to measure the frequency-dependent traveltime difference between observed and simulated seismic arrivals. Measurements are made by cross-correlation or by a frequency-dependent multitaper technique. Our measurement misfit function for a single earthquake is defined by

$$F_e(\mathbf{m}) = \frac{1}{N_e} \sum_{i=1}^{N_e} \left[\Delta T_i(\mathbf{m})\right]^2 / \sigma_i^2 \ , \tag{6.5}$$

where $\mathbf{m}$ is a model vector, N_e denotes the total number of measurement windows for earthquake e, $\Delta T_i(\mathbf{m}) = T_i^{\mathrm{obs}} - T_i^{\mathrm{syn}}(\mathbf{m})$ is the traveltime difference between observed and synthetic waveforms associated with the ith window, and $\sigma_i \geq \sigma_0$ is the associated standard deviation. Our overall misfit function F is simply

$$F(\mathbf{m}) = \frac{1}{E} \sum_{e=1}^{E} F_e(\mathbf{m}) \ , \tag{6.6}$$

where E is the number of earthquakes. Implicit in Equation (6.6) are the choices of the L2-norm and an associated diagonal data covariance matrix $\mathbf{C}_{\mathrm{D}}$ containing terms of E, N_e, and σ_i.

6.4 Misfit gradient and iterative inversion procedure

A distinguishing feature of adjoint tomography is that the gradient of F_e (Eq. 6.5) is computed from an interaction between two wavefields: the "regular" forward simulation emanating from the earthquake source, and the "adjoint" simulation emanating from stations

(*Tarantola*, 1984; *Tromp et al.*, 2005; *Tape et al.*, 2007). The method we use for iterating from the initial model ($\mathbf{m}_{00}$) to the final model ($\mathbf{m}_{16}$) is adapted from the approach illustrated in *Tape et al.* (2007). The *Tape et al.* (2007) study involved a 2D tomographic problem using only synthetic seismograms, whereas the current study is 3D and uses real data. In the 3D problem, our model vector $\mathbf{m}$ contains two variables that describe the structure, V_S and V_B. Finally, our misfit measure is a frequency-dependent multitaper traveltime difference, made using three different period ranges (6–30 s, 3–30 s, 2–30 s).

Our main computational cost involves computing the gradient of F_e (one for each earthquake), which we call an "event kernel" (*Tape et al.*, 2007). In *Tape et al.* (2007) we combined the event kernels by summing them, and then used a conjugate-gradient algorithm to obtain a model update. In this study, we use a subspace projection technique to compute the model update. Instead of using a subspace of model parameter classes (*Kennett et al.*, 1988; *Sambridge et al.*, 1991), we use a subspace of earthquake sources. The basic idea is to determine a linear combination of event kernels that exploits the features they have in common. This procedure provides a preconditioner for the gradient algorithm that increases convergence of the minimization problem. Not all earthquakes were used in each iteration (Table 6.5). This is because for certain iterations, the event kernels were much stronger in specific regions of the model, indicating that the majority of the observed misfit was originating in those regions. The model updates for these iterations did not change appreciably with the inclusion of all event kernels (although the computation time increased considerably).

6.4.1 Computational demands

The computational demands of adjoint tomography are formidable, due to the number of simulations needed to evaluate the misfit function and its gradient at every iteration. Our simulation region is 639 km × 503 km at the surface and extends to 60 km depth (Figure 6.1). For each earthquake we calculated four minutes of seismograms that are accurate down to a period of two seconds. Each simulation took approximately 43 minutes (of wall-clock time) on 168 cores of a parallel computer. For each earthquake we performed three simulations, one to evaluate the misfit function (Eq. 6.5) and two to compute its gradient. Each model iteration thus required $3E_k$ simulations, where E_k is the number of earthquakes used for the kth iteration. The total number of 168-core simulations used in producing model $\mathbf{m}_{16}$

was 6794, totaling 0.8 million CPU-hours. Tabulations of these simulations are shown in Table 6.5 and discussed next.

Table 6.5 lists the number of forward simulations used in constructing the final tomographic model. The total number includes: (1) both sets of earthquake source inversions (at models $\mathbf{m}_{00}$ and $\mathbf{m}_{12}$), (2) forward simulations that were used to construct kernels used in the inversion, (3) forward simulations for 91 earthquakes that were not used in the tomographic inversion, and (4) forward simulations that were used in constructing some kernels that were not used in computing the model update. For each computed kernel, we list "3" as the number of forward simulations performed; it would be possible, in theory, to reduce this number to "2" if we were to hold the final snapshot of the forward wavefield in memory on the parallel computer while computing the misfit function and adjoint sources, prior to creating the adjoint wavefield (*Liu and Tromp*, 2006).

The total number of simulations per earthquake is listed in the fourth column of Table 6.5: a total of 6794 168-core simulations. The number of CPU-hours per earthquake is then the product of the following parameters: number of cores per simulation, number of simulations, duration of simulation (seismogram hours), seismogram-to-wall-clock factor. For our simulations we use 168 cores, and for the desired accuracy of periods of 2 s, the simulation-to-wall-clock-factor is about 13. For example, 300 s of seismograms requires 65 minutes (13×300 s) of wall-clock time. The total for all 6794 simulations is then 0.80 million CPU-hours.

6.5 New 3D crustal model

We present our new crustal model on both relative and absolute scales. First, the update to the seismological model (the relative scale) reveals the changes to the initial SCEC model that are required by the data. We compute the update as $\ln(\mathbf{m}_{16}/\mathbf{m}_{00})$. Second, the seismological model itself reveals the "absolute" model parameters (e.g., wavespeed in units of km/s) and is more relevant for geologic and geodynamic interpretations. All cross sections discussed below are of shear wavespeed (V_S) models ($\mathbf{m}_{00}$ and $\mathbf{m}_{16}$). The bulk sound speed model is discussed in Section 6.5.2.

Figure 6.3 shows the iterative improvement of a single three-component seismogram for an earthquake source beneath the southern San Joaquin basin recorded in the eastern

Mojave. The evolution of the particle motion from $\mathbf{m}_{00}$ to $\mathbf{m}_{16}$ is illustrated by the red synthetic seismograms. The varying time windows are a reminder that the measurement windows may change at each iteration as the fit improves (*Maggi et al.*, 2009). The initial traveltime difference (or "time shift") for the Rayleigh wave in the standard 1D southern California model is 9.60 s on the vertical component (Z) and 9.85 s on the radial component (R). In the initial SCEC model ($\mathbf{m}_{00}$; Figure 6.3b), the Rayleigh wave time shift is 7.00 s (Z) and 7.30 s (R). After 16 iterations, the time shifts are 0.95 s (Z) and 1.00 s (Z). The evolution of the transverse component is more dramatic, as there is virtually no energy between 110 s and 140 s in the SCEC model, and thus there is no time shift to identify. After 16 iterations, the time shift is 0.05 s, and the synthetic transverse-component seismogram captures the main shape of the waveform up to 130 s.

Having demonstrated reasonable fits on all three components, we examine the net change between the initial and final models that resulted in the misfit reduction (Figure 6.3a). The tomographic update, $\ln(\mathbf{m}_{16}/\mathbf{m}_{00})$, contains three principal features. First, there is the addition of the southern San Joaquin basin (*Goodman and Malin*, 1992), marked as a -35% (slow) anomaly immediately above the earthquake source. The basin resonates, influencing the Love wave observed after 110 s. Second, the shear wavespeed of the western Mojave is increased in the upper 3 km, decreased in the depth range 5 km to 15 km, and increased in the depth range 18 km to 26 km. Third, east of the Camp Rock fault, there is a -10% change in wavespeed, probably associated with Quaternary volcanism (*Luffi et al.*, 2009). Only through multiple iterations is it possible to isolate the locations and amplitudes of these changes.

In Figure 6.4, we highlight the improvement in fits for two additional earthquakes. We first consider a Parkfield earthquake on the San Andreas fault recorded at station WGR, north of the Ventura basin (Figure 6.4b). The synthetics for the final model exhibit improved fit of amplitude and phase for both the Rayleigh wave arrival (Z and R: 75–100 s) and the Love wave arrival (T: 60–90 s). In comparison to the 1D and $\mathbf{m}_{00}$ synthetics, the $\mathbf{m}_{16}$ synthetics constitute a dramatic improvement.

We also observe improved fits within the region containing the higher-resolution basin models (*Komatitsch et al.*, 2004). Figure 6.4d shows the improvement in fits for an earthquake that was not used in the tomographic inversion. The seismic wavefield interacts with the Los Angeles and Ventura basins before reaching station STC. The SCEC model captures

the resonance, duration, and approximate amplitude of the observed seismogram, but the final 3D model is markedly better. In particular, we note that the fits for the amplitudes are improved, even though amplitude differences are not built into the misfit function. This demonstrates that the 3D structural changes to the initial model induce additional focusing and amplification of the seismic wavefield.

We emphasize five key points about the model updates (Figure 6.5):

1. The net changes in the model are large, locally in excess of $\pm 30\%$, but the changes during any one iteration are small, locally less than $\pm 10\%$.

2. The areas in the initial model that require changes are highly variable and generally unknown. For example, it takes more than ten iterations to isolate the -35% anomaly related to the southern San Joaquin basin.

3. Although only traveltime differences are used in the misfit function (Eq. 6.5), amplitude differences also decrease in the final model, due to 3D effects of focusing (Figures 6.4d and 6.8).

4. Frequency-dependent surface waves are necessary to resolve crustal structure (Figure 6.3).

5. We are able to use more seismograms for measurements as we improve the seismological model.

We now illustrate model $\mathbf{m}_{16}$ with four additional paths (Figure 6.7). Figure 6.7a shows a striking three-component seismogram of an earthquake that originated near the base of the Salton trough recorded at LA basin station LAF. This path is important for seismic hazard assessments, since large earthquakes have occurred in the past along the southern San Andreas (*Olsen et al.*, 2006). The synthetic seismograms capture the phase and amplitude of most of the first 180 s of the observed records.

We also capture wave propagation effects that occur far from the direct path between the earthquake and station. The three windows in Figure 6.7b highlight three different Rayleigh-wave paths from the earthquake (near Hollywood) to station RVR. The latter two waveforms are not apparent in the synthetics for the initial 3D model. Inclusion of such waveforms in the tomographic inversion shows we can increase the coverage by exploiting additional information already present in the seismograms.

Waveform fits for the shortest period range, 2–30 s, are shown in Figure 6.7c–d. Most of the body-wave pulses in Figure 6.7c fit the observed pulses to within 1 s (our target value). The downward pulse at 33 s on the transverse component of the $\mathbf{m}_{16}$ synthetic seismogram is not apparent in the corresponding $\mathbf{m}_{00}$ synthetic seismogram. Seismograms for a path crossing the entire Mojave (*Fuis et al.*, 2003) are shown in Figure 6.7d. These seismograms match the Love wave at 68 s (T), the P wave at 30 s (Z and R), the Rayleigh wave at 75 s (Z and R), and some additional complexity, particularly on the radial component.

6.5.1 Connections with geology and tectonics

Within a single vertical cross section for a path crossing the Mojave region (Figure 6.3a), we identify reductions in wavespeed due to both compositional and thermal features: above the earthquake source is the southern San Joaquin sedimentary basin (*Goodman and Malin*, 1992), and east of the Camp Rock fault (and north of 34.3°N) there is higher heat flow (*Bonner et al.*, 2003) likely related to Quaternary volcanism (e.g., *Luffi et al.*, 2009, Figure 1). West of the Camp Rock fault, slow wavespeeds and high heat flow are not observed at the surface, nor is volcanic activity.

The middle panels of the horizontal cross sections (Figure 6.5) reveal lateral variations in the new crustal model. At 2 km depth, large-scale slow regions (<2.8 km/s) reveal several known Neogene basins (Figure 6.1a). The fastest regions (>3.5 km/s) occur in the Peninsular Ranges west of the Elsinore fault, and in the Sierra Nevada west of the Kern Canyon fault (*Shapiro et al.*, 2005). The eastern front of the Sierra Nevada is marked by an eastward step in wavespeed from about 3.5 km/s to 2.8 km/s, with the Coso geothermal region and the sedimentary fill in Owen's Valley and Indian Wells Valley accounting for the slower wavespeeds. We attribute the slow wavespeeds (2.9 km/s) in the eastern Mojave to Quaternary volcanism.

At 10 km depth in our crustal model (Figure 6.5b), some of the basins are no longer visible (Los Angeles, Salton trough), and a striking pattern of wavespeeds west of the San Andreas fault is evident. The Peninsular Ranges and a magmatic layer beneath the Salton trough (*Fuis and Kohler*, 1984) form a fast region (3.8 km/s) that is separated by the San Andreas fault from slower regions (3.4 km/s) to the northeast. The 50-km-scale variations in wavespeeds along the longitudinal line 119°N illuminate, from north to south, the western Sierra Nevada (fast), the southern San Joaquin basin (slow), the San Gabriel Mountains

(fast), the Ventura basin (slow), the Santa Monica Mountains (fast), and the Santa Monica basin (slow). Wavespeeds in the Coast Ranges are slowest (3.1 km/s) east of the San Andreas (*Bleibinhaus et al.*, 2007) and along the coast, and are somewhat faster (3.4 km/s) in between, where Mesozoic granitic and sedimentary rocks are exposed at the surface. The northwestern Mojave is slow (3.3 km/s) compared to faster material (3.6 km/s) in the southern Sierra Nevada, across the Garlock fault.

At 20 km depth (Figure 6.5c) the most striking feature is the fast wavespeed region (4.1 km/s) beneath the Ventura–Santa Barbara basin and the Santa Monica Mountains, also observed in Figure 6.4c. This region coincides with the surface expression of the western Transverse Ranges block (WTRB *Luyendyk et al.*, 1980) (Figure 6.1a), bound to the north by the Santa Ynez fault and to the south by the Malibu Coast fault. We interpret this feature as subduction-captured Farallon oceanic crust, on top of which the WTRB rotated clockwise by more than 90° from a position near the Peninsular Ranges (3.8 km/s) (*Nicholson et al.*, 1994). It is possible that the WTRB crustal anomaly is related to upper mantle anomalies observed below this region (*Humphreys and Clayton*, 1990).

6.5.2 Bulk sound speed model

Horizontal cross sections of the bulk sound speed (V_B) models are shown in Figure 6.6. At 20 km and 10 km depths, the larger spatial extent of the masked region indicates that our sensitivity to V_B is not as good as at shallow depths.

At 2 km depth the initial 3D model, V_B $\mathbf{m}_{00}$, contains considerable spatial variations that are also present in the final model, because our perturbation contains only longer scalelength variations. Our perturbation, $\ln(\mathbf{m}_{16}/\mathbf{m}_{00})$, is almost uniformly negative, indicating that the bulk-sound speed—on the whole—is too fast in the initial model.

Outside the Los Angeles basin, the slowest feature in the initial model is near Indian Wells Valley, just south of the Coso geothermal region (e.g., *Hauksson and Unruh*, 2007). Our model update applies a -15% change in V_B to this anomaly. Interestingly, in the central Mojave region at 2 km depth, the change to V_B is about -10% (Figure 6.6a), whereas the change to V_S is about $+5\%$ (Figure 6.5a). These changes of opposite sign will lead to more pronounced changes in quantities such as Poisson's ratio and the $V_\mathrm{P}/V_\mathrm{S}$ ratio (e.g., *Christensen*, 1996).

6.5.3 Implications for seismic hazard assessment

Our results demonstrate that moderate (M_w = 3.5–5.5), well-recorded earthquakes (Figure 6.1) can be used to make large, necessary changes to the crustal model of southern California. Waveforms from these earthquakes can be extremely complicated, even at relatively long periods (6–30 s). One example is the path from the Salton trough to the Los Angeles basin (Figure 6.7a), the same region covered by the TeraShake simulations (*Olsen et al.*, 2006).

If it is not possible to fit waveforms from moderate, point-source earthquakes, then it will not be possible to fit waveforms from large earthquakes with complex ruptures. By beginning to fit complex propagation paths for moderate earthquakes, we provide hope for accurately simulating larger earthquakes. For example, the transverse-component ground motion from a M_w 4.5 earthquake on the White Wolf fault (Figure 6.3) is not apparent in the simulations based upon the initial 3D model, but is present in those based upon the final model. The new model therefore provides a better starting point for simulating larger earthquakes on the White Wolf fault, such as the 1952 M_w 7.2 Kern Country earthquake. Similarly, the improvement in fits for the M_w 4.6 Parkfield earthquake (Figure 6.3) suggests that the new crustal model is more appropriate for simulations of larger earthquakes on this segment of the San Andreas fault, such as the 1857 M_w 7.9 Fort Tejon earthquake.

In southern California, there are no high-quality seismic waveforms available for major "scenario" earthquakes, that is, earthquakes that have occurred in the past and that are likely to reoccur in the future (*Olsen et al.*, 2006). However, there are several strong (M_w = 6–7) earthquakes that have been recorded well enough to determine rupture models (*Custódio et al.*, 2005). These earthquakes present the formidable challenge of fitting near-source and regional waveforms that capture the complexities of both the rupture process and the heterogeneous structure. Our more accurate 3D crustal model will benefit the development of rupture models for strong earthquakes.

An improved crustal model will allow for the systematic search for "exotic" seismic waveforms that result from wave propagation in complex 3D structure that may contain interfaces at all possible orientations. This search should be undertaken in the regions with the strongest heterogeneity, including surface topography variations (*Ma et al.*, 2007; *Lee et al.*, 2008), and emphasis should be placed on waveforms with anomalous amplitude,

indicative of damaging energy. It is likely that quantities such as the maximum amplitude of ground motion at a particular location will likely be extremely sensitive to changes in source–station geometry. In the same manner in which we can illuminate the sensitivity region of a Pn head wave (*Liu and Tromp*, 2006), we should be able to also illuminate the region of more exotic waves.

6.6 Misfit analysis

In Figure 6.3 we illustrated the misfit reduction for one particular path between an earthquake source and a station. Our overall assessment of the misfit reduction from the initial SCEC model to the final model is based on 12,583 different paths (Table 6.4). This assessment cannot be based simply on a traveltime misfit function, because there are many seismic waveforms in the final model that do not have a measurable traveltime difference in the initial model (e.g., Figure 6.3b). Thus, in order to facilitate a direct comparison between the two models, we compute a simple waveform difference using the time windows that were selected for the final model for the 143 earthquakes used in the tomographic inversion (Figure 6.8a).

We also consider a separate set of 91 earthquakes that was not used in the tomographic inversion. An earthquake not used in the tomographic inversion—or any future earthquake, for that matter—may be used to independently assess the misfit reduction from $\mathbf{m}_{00}$ to $\mathbf{m}_{16}$. Remarkably, the reduction in waveform difference misfit for the extra earthquakes is almost the same as it is for the earthquakes used in the inversion (Figure 6.8). This result provides validation for the tomographic model and suggests that future earthquakes will see the same misfit reduction.

Many of the 91 earthquakes occur in similar regions to the 143 earthquakes (Figure 6.2), and thus one might argue that the misfit reduction would be similar, since the paths are similar to those used in the tomographic inversion. We would agree to some extent, but would counter with two points. First, even for near-identical paths, the occurrence of similar misfit confirms the quality of the initial uninverted source parameters (focal mechanism, origin time, hypocenter). This is a critical aspect of the tomographic inversion, that we are (for the most part) not mapping seismogram misfit due to source errors into structure changes; these consequences are illustrated in (*Tape et al.*, 2007, Figure 19b). Second,

"similar" paths—in the sense of a "nearby" earthquake recorded at the same station—may not be very similar in regions of strong heterogeneity. A change of source location (or station location, for that matter) of 2 km can have a profound impact on seismic waveforms, especially at higher frequencies.

6.6.1 Waveform misfit, $F_{\mathrm{w}}(\mathbf{m})$

We use a direct waveform difference, $F_{\mathrm{w}}(\mathbf{m})$ (Eq. 6.4), as the primary measure of misfit. In tabulating the histograms in Figure 6.8, we exclude all windows whose time shifts in *both* $\mathbf{m}_{00}$ and $\mathbf{m}_{16}$ are ≤ 1 s, our target measurement value in the tomographic problem. This leaves behind only those windows that have changed appreciably (for better or for worse). The waveform misfit measure is applied to either the portions of records within the time windows (Figure 6.8a, c) or to the entire seismogram containing at least one (non-excluded) time window (Figure 6.8b, d), including time before the expected P-wave arrival and after the surface wave arrivals. For a given set of windows, the number of seismograms containing windows will be less than (or equal to) the number of windows. The number of seismograms listed includes (up to three) different bandpassed versions.

The waveform misfit analysis is shown in Figure 6.8. There are several comparisons to make among the subplots.

1. There is a strong similarity between the earthquakes used in the inversion ("tomo") and the earthquakes not used in the inversion ("extra"). (In some cases, the "extra" earthquakes actually display a better misfit reduction than the "tomo" earthquakes.)

2. The waveform misfit of the full seismograms (Figure 6.8b, d) is reduced.

3. The waveform misfit of the measurement windows is better than that computed for the full seismograms, as expected.

4. For the measurement windows, neither the overall misfit nor the misfit reduction show a dependence on period range. This is not a one-to-one comparison, since the comparison is for different sets of windows, but it suggests that for many windows, such as those common to all three period ranges, the synthetic waveforms are capturing the dominant features of the wavefield. For the full seismograms, however, both the misfit and misfit reduction get progressively better from 2–30 s to 3–30 s to 6–30 s.

This is because measurement windows selected on the 6–30 s records cover more of the full seismogram than those selected on the 3–30 s and 2–30 s records, and thus we expect more of a misfit reduction.

6.6.2 Traveltime misfit, $F_t(\mathbf{m})$

We use a multitaper traveltime difference, $F_t(\mathbf{m})$ (Eq. 6.3), within the tomographic inversion. The traveltime differences in the final model have a standard deviation of less than 1 s for the entire dataset (Figure 6.9). In other words, given an adequate location, origin time, and focal mechanism for any $M_w = 3.5$–5.5 earthquake in southern California, we expect most traveltime differences computed using our crustal model to be ≤ 1 s for seismic records in the period range 2–30 s. For the three period ranges, the patterns do not change appreciably, and all listed standard deviations of the time shifts are <0.8 s (Figure 6.9).

6.7 Resolution considerations

We compute the composite volumetric sensitivity of all measurements (e.g., *Chen et al.*, 2007). This is achieved by using the same procedure that was used to compute each event kernel (*Tape et al.*, 2007), and omitting the traveltime measurement weight for each adjoint source (*Tromp et al.*, 2005). Because we have two inversion variables, V_S and V_B, we also have two corresponding volumetric sensitivity kernels, which we refer to as "coverage kernels" for brevity.

Coverage kernels for V_S and V_B are shown in Figures 6.10 and 6.11. The left column shows the field without the mask, and the right column includes the mask. The threshold for the mask is given by a subjective value of $K_0 = 10^{-16}$ m^{-3}. In regions where the coverage kernel is less than this value, the tomographic model is masked out, as shown in Figure 6.10. The coverage kernel decreases with depth, and has maximum sensitivity near the surface, which is sampled by the shorter-period surface waves in the dataset. The masks shown in Figure 6.10 are applied to the V_S cross sections shown in Figure 6.5. The coverage kernel for V_B contains lower amplitudes, leading to larger masks in Figure 6.11. These masks are applied to the V_B cross sections shown in Figure 6.6.

A seismic tomographic study will typically include a resolution analysis that shows how well a model perturbation (e.g., a delta function or a checkerboard pattern) is expected

to be resolved by the inversion procedure. These representations, however, are limited by the forward model embedded within the inverse problem. If the forward model is a simple computation (such as with ray theory), then it is possible to perform resolution tests with limited additional computation.

In our case, the forward model is computationally expensive, and a resolution test would require a comparable number of simulations as the real problem. Instead of a formal resolution analysis, we qualitatively examine the model update $\ln(\mathbf{m}_{16}/\mathbf{m}_{00})$, which provides estimates of the resolvable scalelengths in our problem. In particular, the minimum scalelength is about 2 km in depth (visible in Figure 6.3a) and about 6 km laterally. These values correspond to the regions of densest coverage, and lower resolution is expected in regions of poor coverage, such as the Great Valley or near the boundaries of the simulation region. We note that shorter scalelength features are present in the unsmoothed event kernels, but our choices of regularization prevent them from appearing in the model updates. In other words, we adopt a conservative approach that will introduce the finer details into the model only if seismograms from many different earthquakes require them.

We advocate monitoring the uncertainty of model parameters rather than conducting formal resolution analyses, because the former can be achieved without repeating the full inverse problem. Future work will address the uncertainties of model parameters. From a Bayesian perspective, our final model ($\mathbf{m}_{16}$) represents the mean model of a posterior distribution of possible models ($\mathbf{C}_{\mathrm{M}}$) (*Tarantola*, 2005). It is important that we construct a distribution of possible models that provides a guide for future studies that inevitably will include more stations and higher-frequency seismograms. The inclusion of additional data will then help reduce the distribution of all possible models. One promising approach to considering uncertainties of model parameters is the square-root variable metric method. Using this method it is possible to obtain *samples* of the posterior distribution $\mathbf{C}_{\mathrm{M}}$ without computing the prohibitively large $M \times M$ $\mathbf{C}_{\mathrm{M}}$ itself.

6.8 Summary

In this study we have exploited the accuracy of the SEM (*Komatitsch and Vilotte*, 1998; *Komatitsch et al.*, 2004) within an inverse problem. After 16 iterations, we have obtained a model with local perturbations of $\pm 30\%$ from the initial 3D model. We have fit thousands

of three-component waveforms that capture both the phase and amplitude of the particle motion at the stations. Direct waveform difference measurements of full-length seismograms that were never used in the inversion (Figure 6.8b, d) provide compelling support for the quality of the new crustal model. The ability to capture "exotic" seismic waveforms, such as from basin resonance (Figure 6.4b) and from laterally reflected surface waves (Figure 6.7b; also *Stich et al.* (2009)), suggests the prospect of enhancing tomographic images by delving deeper into the seismic records.

Seismic studies indicate the possible presence of interfaces at all scales and all possible orientations (*Ni et al.*, 2002; *Fuis et al.*, 2003; *Bleibinhaus et al.*, 2007). Interfaces in our tomography model that were sharp to begin with—the topography surface, the basement surface, and the Moho—remain sharp in the final model, since we only allow relatively smooth changes to the model. However, it is clear that the model update illuminates several features that appear to be sharp, including the southern San Joaquin basin and the eastern margin of the Sierra Nevada. And it is also clear from previous studies that interfaces such as the Moho are not uniformly sharp (*Mori and Helmberger*, 1996). The next stage of improving the model will be to numerically implement the most robust interfaces, and to check for the improvement of fits to seismograms, in particular for reflected phases from the interfaces.

Our new tomographic model for southern California is described in terms of shear-wave and bulk-sound speeds. The topography of primary interfaces (Moho and basement surface) remains fixed, anisotropy is not permitted, and attenuation does not change. These are all parameters that are specified in the forward model but are not used in the inverse problem, and they constitute future possible extensions of this research. Sensitivity kernels for anisotropic parameters (*Sieminski et al.*, 2007) and boundary surfaces (*Tromp et al.*, 2005; *Liu and Tromp*, 2008) are already available for the inverse problem, but there will be challenges in implementing multiple classes of model parameters.

Table 6.1: Standard 1D reference model for southern California (*Kanamori and Hadley*, 1975; *Dreger and Helmberger*, 1990; *Wald et al.*, 1995). V_B is listed for comparison and is computed via $V_B^2 = V_P^2 - \frac{4}{3}V_S^2$. The Moho depth of 32 km is from *Wald et al.* (1995). The listed 60 km base level is based on our numerical simulation region.

layer	top m	bottom m	thickness m	V_P m s^{-1}	V_B m s^{-1}	V_S m s^{-1}	ρ kg m^{-3}
1	0	5500	5500	5500	4095	3180	2400
2	5500	16000	10500	6300	4693	3640	2670
3	16000	32000	16000	6700	4992	3870	2800
4	32000	60000	28000	7800	5817	4500	3000

Table 6.2: Values of parameters used for the window-picking code FLEXWIN (*Maggi et al.*, 2009), based on the synthetics for the final model $\mathbf{m}_{16}$.

$T_{0,1}$	6, 30	3, 30	2, 30
$r_{P,A}$	3.0, 2.5	2.5, 3.5	2.5, 3.5
r_0	3.0	4.0	4.0
w_E	0.18	0.11	0.07
CC_0	0.71	0.80	0.85
$\Delta\tau_0$	4.0	3.0	2.0
$\Delta \ln A_0$	1.5	1.0	1.0
$\Delta\tau_{\mathrm{ref}}$	0.0	0.0	0.0
$\Delta \ln A_{\mathrm{ref}}$	0.0	0.0	0.0
c_0	0.7	1.3	1.0
c_1	2.0	4.0	5.0
c_2	0.0	0.0	0.0
$c_{3a,b}$	3.0, 2.0	4.0, 2.5	4.0, 2.5
$c_{4a,b}$	2.5, 12.0	2.0, 6.0	2.0, 6.0
$w_{\mathrm{CC}}, w_{\mathrm{len}}, w_{\mathrm{nwin}}$	0.5,1.0,0.7	0.70,0.25,0.05	1,1,1

Table 6.3: Summary of the tomographic inversion, based only on seismograms with measurements for the final model $\mathbf{m}_{16}$. "TOMO" corresponds to the 143 earthquakes used in the tomographic inversion (Table 1). "EXTRA" corresponds to the 91 extra earthquakes not used in the tomographic inversion. "COMBINED" corresponds to the TOMO+EXTRA set of 243 earthquakes. The number of unique seismograms is indicated next to "seismograms (unique)". The number of total seismograms—including the three 6–30 s, 3–30 s, and 2–30 s—is indicated next to "seismograms (total)". The same is true for "windows (total)". A "path" is a single source-station pair that has at least one measurement.

	TOMO	EXTRA	COMBINED
components (Z,R,T)	3	3	3
networks	8	7	8
earthquakes	**143**	**91**	**234**
stations	203	200	210
paths	12583	4305	16888
seismograms (unique)	27007	8013	35020
seismograms (total)	52138	14803	66941
windows (total)	61673	16758	78431

Table 6.4: Summary of seismogram measurement time windows for final model $\mathbf{m}_{16}$. Each entry corresponds to the number of measurement windows for a particular period range of data (6–30 s, 3–30 s, 2–30 s) for a particular component (Z, R, T).

	6–30 s	3–30 s	2–30 s	total
vertical (Z)	10319	5623	4864	20806
radial (R)	9276	5443	4579	19298
transverse (T)	10657	5684	5228	21569
total	30252	16750	14671	61673

Table 6.5: Tabulation of simulations for each earthquake and each model iteration. The description of each column is listed below, with the values in the subsequent table, with the totals for each column listed in the final row. The label "relocation available" indicates whether a relocated hypocenter (with origin time) was available for the earthquake (e.g., *Lin et al.*, 2007a; *Thurber et al.*, 2006).

column	label	description
1		index
2	`eid`	earthquake ID (Southern California Earthquake Data Center)
3	`dur`	duration of computed seismograms in seconds (120, 200, 300)
4	`Ne`	total number of forward simulations for earthquake
5	`m00`	number of forward simulations performed at $\mathbf{m}_{00}$: `1` = synthetics only; `3` = kernel (not used); `*3` = kernel (used)
6	`S00`	number of forward simulations performed for source inversion at $\mathbf{m}_{00}$: `6` = SEM inversion; `0` = no SEM inversion
7	`m01`	number of forward simulations performed at $\mathbf{m}_{01}$
⋮	⋮	⋮
18	`m12`	number of forward simulations performed at $\mathbf{m}_{12}$
19	`S12`	number of forward simulations performed for source inversion at $\mathbf{m}_{12}$: `6` = SEM inversion; `0` = no SEM inversion
20	`m13`	number of forward simulations performed at $\mathbf{m}_{13}$
⋮	⋮	⋮
23	`m16`	number of forward simulations performed at $\mathbf{m}_{16}$
24		relocation available (`Y` or `N`)
25		earthquake used in at least one model update (`TOMO`) or kept as an extra earthquake for misfit analysis(`EXTRA`)

	eid	dur	Ne	m00	S00	m01	m02	m03	m04	m05	m06	m07	m08	m09	m10	m11	m12	S12	m13	m14	m15	m16		
1	9967025	200	26	*3	0	*3	*3	*3	*3	1	0	0	0	0	0	0	0	6	0	1	0	3	Y	TOMO
2	9967137	200	10	1	0	0	0	0	0	1	0	0	0	0	0	0	0	6	0	1	0	1	Y	EXTRA
3	9967249	200	10	1	0	0	0	0	0	1	0	0	0	0	0	0	0	6	0	1	0	1	Y	EXTRA
4	9967901	300	49	*3	6	*3	*3	*3	*3	*3	*3	1	0	0	0	0	3	6	*3	*3	*3	3	Y	TOMO
5	9968977	300	63	*3	6	*3	*3	*3	*3	*3	*3	*3	*3	*3	*3	*3	*3	6	*3	*3	*3	3	Y	TOMO
6	14096736	300	63	*3	6	*3	*3	*3	*3	*3	*3	*3	*3	*3	*3	*3	*3	6	*3	*3	*3	3	Y	TOMO
7	14189556	200	25	1	6	0	0	0	0	1	0	1	0	0	0	0	1	6	0	*3	*3	3	Y	TOMO
8	14263252	120	4	1	0	0	0	0	0	1	0	0	0	0	0	0	0	0	0	1	0	1	N	EXTRA
9	14095540	300	63	*3	6	*3	*3	*3	*3	*3	*3	*3	*3	*3	*3	*3	*3	6	*3	*3	*3	3	Y	TOMO
10	14096196	300	49	1	6	0	0	0	0	*3	*3	*3	*3	*3	*3	*3	*3	6	*3	*3	*3	3	Y	TOMO
11	10063349	300	39	*3	6	*3	*3	*3	*3	1	0	1	0	0	0	0	1	6	0	*3	*3	3	Y	TOMO
12	10100053	300	60	*3	6	*3	*3	*3	*3	*3	*3	*3	*3	*3	3	0	*3	6	*3	*3	*3	3	Y	TOMO
13	9171679	120	39	*3	6	*3	*3	*3	*3	1	0	1	0	0	0	0	3	6	0	*3	1	3	Y	TOMO
14	9983429	300	63	*3	6	*3	*3	*3	*3	*3	*3	*3	*3	*3	*3	*3	*3	6	3	*3	*3	3	Y	TOMO
15	14138080	300	63	*3	6	*3	*3	*3	*3	*3	*3	*3	*3	*3	*3	*3	*3	6	3	*3	*3	3	Y	TOMO
16	10097009	200	36	*3	6	*3	1	0	0	1	0	1	0	0	0	0	*3	6	3	*3	*3	3	Y	TOMO
17	14186612	200	63	*3	6	*3	*3	*3	*3	*3	*3	*3	*3	*3	*3	*3	*3	6	3	*3	*3	3	Y	TOMO
18	14186928	120	10	1	0	0	0	0	0	1	0	0	0	0	0	0	0	6	0	1	0	1	Y	EXTRA
19	9094270	120	3	1	0	0	0	0	0	0	0	0	0	0	0	0	0	0	0	1	0	1	Y	EXTRA
20	9151000	120	26	*3	0	*3	*3	*3	*3	1	0	0	0	0	0	0	0	6	0	1	0	3	Y	TOMO
21	9875657	120	26	*3	0	*3	*3	*3	*3	1	0	0	0	0	0	0	0	6	0	1	0	3	Y	TOMO
22	9875665	120	26	*3	0	*3	*3	*3	*3	1	0	0	0	0	0	0	0	6	0	1	0	3	Y	TOMO

23	9882325	200	60	*3	6	*3	*3	*3	*3	*3	*3	*3	*3	*3	*3	3	6	0	*3	*3	3	Y	TOMO
24	9882329	200	43	*3	6	*3	*3	*3	*3	3	0	1	0	0	0	0	3	6	0	*3	*3	3	Y	TOMO
25	14095628	200	60	*3	6	*3	*3	*3	*3	*3	*3	*3	*3	*3	*3	*3	3	6	0	*3	*3	3	Y	TOMO
26	14187364	120	26	*3	0	*3	*3	*3	*3	1	0	0	0	0	0	0	0	6	0	1	0	3	Y	TOMO
27	9095528	200	3	1	0	0	0	0	0	0	0	0	0	0	0	0	0	0	0	1	0	1	Y	EXTRA
28	9151609	200	41	*3	6	*3	*3	*3	*3	1	0	1	0	0	0	0	3	6	0	*3	*3	3	Y	TOMO
29	9644345	200	60	*3	6	*3	*3	*3	*3	*3	*3	*3	*3	*3	*3	*3	3	6	0	*3	*3	3	Y	TOMO
30	9653293	200	3	1	0	0	0	0	0	0	0	0	0	0	0	0	0	0	0	1	0	1	Y	EXTRA
31	9653349	200	3	1	0	0	0	0	0	0	0	0	0	0	0	0	0	0	0	1	0	1	Y	EXTRA
32	9653493	200	63	*3	6	*3	*3	*3	*3	*3	*3	*3	*3	*3	*3	*3	6	3	*3	*3	3	Y	TOMO
33	12887732	120	60	*3	6	*3	*3	*3	*3	*3	*3	*3	*3	*3	*3	3	6	0	*3	*3	3	Y	TOMO
34	9915909	120	3	1	0	0	0	0	0	0	0	0	0	0	0	0	0	0	1	0	1	Y	EXTRA
35	13986104	200	38	*3	6	*3	*3	*3	*3	1	0	1	0	0	0	0	3	6	0	3	0	3	Y	TOMO
36	9994573	120	26	*3	0	*3	*3	*3	*3	1	0	0	0	0	0	0	0	6	0	1	0	3	Y	TOMO
37	14169456	200	60	*3	6	*3	*3	*3	*3	*3	*3	*3	*3	*3	*3	*3	3	6	0	*3	*3	3	Y	TOMO
38	9044494	120	3	1	0	0	0	0	0	0	0	0	0	0	0	0	0	0	1	0	1	Y	EXTRA
39	3298170	200	3	1	0	0	0	0	0	0	0	0	0	0	0	0	0	0	1	0	1	Y	EXTRA
40	9044650	200	3	1	0	0	0	0	0	0	0	0	0	0	0	0	0	0	1	0	1	Y	EXTRA
41	9045109	200	3	1	0	0	0	0	0	0	0	0	0	0	0	0	0	0	1	0	1	Y	EXTRA
42	9045697	120	3	1	0	0	0	0	0	0	0	0	0	0	0	0	0	0	1	0	1	Y	EXTRA
43	9116921	200	41	*3	6	*3	*3	*3	*3	1	0	1	0	0	0	0	3	6	0	*3	*3	3	Y	TOMO
44	7179710	200	41	*3	6	*3	*3	*3	*3	1	0	1	0	0	0	0	3	6	0	*3	*3	3	Y	TOMO
45	9141142	120	30	*3	6	*3	*3	1	1	1	0	1	0	0	0	0	1	6	0	1	0	3	N	TOMO
46	7180136	200	3	1	0	0	0	0	0	0	0	0	0	0	0	0	0	0	1	0	1	Y	EXTRA
47	9163702	200	3	1	0	0	0	0	0	0	0	0	0	0	0	0	0	0	1	0	1	Y	EXTRA
48	9642941	200	3	1	0	0	0	0	0	0	0	0	0	0	0	0	0	0	1	0	1	Y	EXTRA
49	9646589	200	3	1	0	0	0	0	0	0	0	0	0	0	0	0	0	0	1	0	1	Y	EXTRA
50	10964587	200	48	*3	6	*3	*3	*3	*3	*3	*3	*3	3	0	0	0	3	6	0	3	0	3	Y	TOMO
51	9673577	120	3	1	0	0	0	0	0	0	0	0	0	0	0	0	0	0	1	0	1	Y	EXTRA
52	9674049	300	40	*3	6	*3	*3	*3	*3	3	0	1	0	0	0	0	3	6	0	3	0	3	Y	TOMO
53	9674097	200	3	1	0	0	0	0	0	0	0	0	0	0	0	0	0	0	1	0	1	Y	EXTRA
54	9674205	200	3	1	0	0	0	0	0	0	0	0	0	0	0	0	0	0	1	0	1	Y	EXTRA
55	9674213	300	40	*3	6	*3	*3	*3	*3	3	0	1	0	0	0	0	3	6	0	3	0	3	Y	TOMO
56	9674653	200	3	1	0	0	0	0	0	0	0	0	0	0	0	0	0	0	1	0	1	Y	EXTRA
57	10992159	300	48	*3	6	*3	*3	*3	*3	*3	*3	*3	3	0	0	0	3	6	0	3	0	3	Y	TOMO
58	11671240	200	38	*3	6	*3	*3	*3	*3	1	0	1	0	0	0	0	3	6	0	3	0	3	Y	TOMO
59	9686565	200	48	*3	6	*3	*3	*3	*3	*3	*3	*3	3	0	0	0	3	6	0	3	0	3	Y	TOMO
60	9688025	200	3	1	0	0	0	0	0	0	0	0	0	0	0	0	0	0	1	0	1	Y	EXTRA
61	9688709	200	48	*3	6	*3	*3	*3	*3	*3	*3	*3	3	0	0	0	3	6	0	3	0	3	Y	TOMO
62	9828889	200	60	*3	6	*3	*3	*3	*3	*3	*3	*3	*3	*3	*3	*3	3	6	0	*3	*3	3	Y	TOMO
63	9829213	120	41	*3	6	*3	*3	*3	*3	1	0	1	0	0	0	0	3	6	0	*3	*3	3	Y	TOMO
64	10023841	200	3	1	0	0	0	0	0	0	0	0	0	0	0	0	0	0	1	0	1	Y	EXTRA
65	9152038	200	3	1	0	0	0	0	0	0	0	0	0	0	0	0	0	0	1	0	1	Y	EXTRA
66	9165019	120	3	1	0	0	0	0	0	0	0	0	0	0	0	0	0	0	1	0	1	Y	EXTRA
67	9171064	120	10	1	0	0	0	0	0	1	0	0	0	0	0	0	0	6	0	1	0	1	Y	EXTRA
68	9631385	120	10	1	0	0	0	0	0	1	0	0	0	0	0	0	0	6	0	1	0	1	Y	EXTRA
69	14007388	120	38	*3	6	*3	*3	*3	*3	1	0	1	0	0	0	0	3	6	0	*3	0	3	Y	TOMO
70	14204000	120	34	*3	6	*3	*3	*3	1	1	0	1	0	0	0	0	1	6	0	*3	0	3	Y	TOMO
71	14219360	120	41	*3	6	*3	*3	*3	*3	1	0	1	0	0	0	0	3	6	0	*3	*3	3	Y	TOMO
72	14418600	200	3	1	0	0	0	0	0	0	0	0	0	0	0	0	0	0	0	0	1	1	N	EXTRA
73	3320736	300	43	*3	6	*3	*3	*3	*3	3	0	1	0	0	0	0	*3	6	*3	3	0	3	Y	TOMO
74	9109131	120	3	1	0	0	0	0	0	0	0	0	0	0	0	0	0	0	1	0	1	Y	EXTRA
75	9109254	200	3	1	0	0	0	0	0	0	0	0	0	0	0	0	0	0	1	0	1	Y	EXTRA
76	9109287	120	3	1	0	0	0	0	0	0	0	0	0	0	0	0	0	0	1	0	1	Y	EXTRA
77	9109442	120	3	1	0	0	0	0	0	0	0	0	0	0	0	0	0	0	1	0	1	Y	EXTRA
78	9109496	120	3	1	0	0	0	0	0	0	0	0	0	0	0	0	0	0	1	0	1	Y	EXTRA
79	9109636	120	3	1	0	0	0	0	0	0	0	0	0	0	0	0	0	0	1	0	1	Y	EXTRA
80	9110685	200	3	1	0	0	0	0	0	0	0	0	0	0	0	0	0	0	1	0	1	Y	EXTRA
81	9111353	200	43	*3	6	*3	*3	*3	*3	3	0	1	0	0	0	0	*3	6	*3	3	0	3	Y	TOMO
82	9112735	200	46	*3	6	*3	*3	*3	*3	3	0	1	0	0	0	0	*3	6	*3	*3	*3	3	Y	TOMO
83	9113909	200	46	*3	6	*3	*3	*3	*3	3	0	1	0	0	0	0	*3	6	*3	*3	*3	3	Y	TOMO

84	3321590	200	46	*3	6	*3	*3	*3	*3	3	0	1	0	0	0	0	*3	6	*3	*3	*3	3	Y	TOMO
85	3320884	120	46	*3	6	*3	*3	*3	*3	3	0	1	0	0	0	0	*3	6	*3	*3	*3	3	Y	TOMO
86	9114042	120	3	1	0	0	0	0	0	0	0	0	0	0	0	0	0	0	0	1	0	1	Y	EXTRA
87	9114612	120	3	1	0	0	0	0	0	0	0	0	0	0	0	0	0	0	0	1	0	1	Y	EXTRA
88	3324595	120	4	1	0	0	0	0	0	1	0	0	0	0	0	0	0	0	0	1	0	1	Y	EXTRA
89	9114763	120	41	*3	6	*3	*3	*3	*3	1	0	1	0	0	0	0	*3	6	*3	3	0	3	Y	TOMO
90	9114775	120	3	1	0	0	0	0	0	0	0	0	0	0	0	0	0	0	0	1	0	1	Y	EXTRA
91	9114812	200	46	*3	6	*3	*3	*3	*3	3	0	1	0	0	0	0	*3	6	*3	*3	*3	3	Y	TOMO
92	9114858	120	3	1	0	0	0	0	0	0	0	0	0	0	0	0	0	0	0	1	0	1	Y	EXTRA
93	3320951	120	3	1	0	0	0	0	0	0	0	0	0	0	0	0	0	0	0	1	0	1	Y	EXTRA
94	3320940	120	3	1	0	0	0	0	0	0	0	0	0	0	0	0	0	0	0	1	0	1	Y	EXTRA
95	3320954	120	3	1	0	0	0	0	0	0	0	0	0	0	0	0	0	0	0	1	0	1	Y	EXTRA
96	9117942	120	43	*3	6	*3	*3	*3	*3	3	0	1	0	0	0	0	*3	6	*3	3	0	3	Y	TOMO
97	3321426	120	37	*3	6	*3	*3	*3	*3	1	0	1	0	0	0	0	*3	6	1	1	0	3	Y	TOMO
98	9119414	120	4	1	0	0	0	0	0	0	0	0	0	0	0	0	0	0	0	1	1	1	N	EXTRA
99	9120741	120	46	*3	6	*3	*3	*3	*3	3	0	1	0	0	0	0	*3	6	*3	*3	*3	3	Y	TOMO
100	9122706	200	46	*3	6	*3	*3	*3	*3	3	0	1	0	0	0	0	*3	6	*3	*3	*3	3	Y	TOMO
101	9130422	120	39	*3	6	*3	*3	*3	*3	1	0	1	0	0	0	0	*3	6	*3	1	0	3	Y	TOMO
102	7177729	120	46	*3	6	*3	*3	*3	*3	3	0	1	0	0	0	0	*3	6	*3	*3	*3	3	Y	TOMO
103	9147453	120	34	*3	6	*3	*3	*3	*3	1	0	1	0	0	0	0	1	6	0	1	0	3	Y	TOMO
104	9155518	200	46	*3	6	*3	*3	*3	*3	3	0	1	0	0	0	0	*3	6	*3	*3	*3	3	Y	TOMO
105	9775765	200	43	*3	6	*3	*3	*3	*3	3	0	1	0	0	0	0	*3	6	*3	3	0	3	Y	TOMO
106	9805021	120	3	1	0	0	0	0	0	0	0	0	0	0	0	0	0	0	0	1	0	1	Y	EXTRA
107	9854597	200	46	*3	6	*3	*3	*3	*3	3	0	1	0	0	0	0	*3	6	*3	*3	*3	3	Y	TOMO
108	13945908	200	43	*3	6	*3	*3	*3	*3	3	0	1	0	0	0	0	*3	6	*3	3	0	3	Y	TOMO
109	9930549	200	46	*3	6	*3	*3	*3	*3	3	0	1	0	0	0	0	*3	6	*3	*3	*3	3	Y	TOMO
110	14408052	300	3	1	0	0	0	0	0	0	0	0	0	0	0	0	0	0	0	1	0	1	N	EXTRA
111	12659440	200	38	*3	6	1	0	0	0	*3	*3	*3	*3	3	0	0	1	6	0	3	0	3	Y	TOMO
112	10006857	200	60	*3	6	*3	*3	*3	*3	*3	*3	*3	*3	*3	*3	*3	*3	6	3	3	0	3	Y	TOMO
113	14139108	120	10	1	0	0	0	0	0	1	0	0	0	0	0	0	0	6	0	1	0	1	Y	EXTRA
114	14139160	200	10	1	0	0	0	0	0	1	0	0	0	0	0	0	0	6	0	1	0	1	Y	EXTRA
115	14165408	200	35	1	6	0	0	0	0	*3	*3	*3	*3	3	0	0	1	6	0	3	0	3	Y	TOMO
116	7210945	200	4	1	0	0	0	0	0	0	0	0	0	0	0	0	0	0	0	1	1	1	N	EXTRA
117	9695397	200	38	1	6	0	0	0	0	*3	*3	*3	*3	*3	3	0	1	6	0	3	0	3	Y	TOMO
118	9695549	300	18	1	6	0	0	0	0	1	0	1	0	0	0	0	1	6	0	1	0	1	N	EXTRA
119	10148829	200	18	1	6	0	0	0	0	1	0	1	0	0	0	0	1	6	0	1	0	1	N	EXTRA
120	9096972	200	3	1	0	0	0	0	0	0	0	0	0	0	0	0	0	0	0	1	0	1	Y	EXTRA
121	9165761	120	10	1	0	0	0	0	0	1	0	0	0	0	0	0	0	6	0	1	0	1	Y	EXTRA
122	9173365	200	58	*3	6	*3	*3	*3	*3	*3	*3	*3	*3	*3	*3	*3	*3	6	1	3	0	3	Y	TOMO
123	9173374	200	58	*3	6	*3	*3	*3	*3	*3	*3	*3	*3	*3	*3	*3	*3	6	1	3	0	3	Y	TOMO
124	9753485	200	52	*3	6	*3	*3	1	0	*3	*3	*3	*3	*3	*3	*3	3	6	0	3	0	3	Y	TOMO
125	9753489	200	58	*3	6	*3	*3	*3	*3	*3	*3	*3	*3	*3	*3	*3	*3	6	1	3	0	3	Y	TOMO
126	9753497	200	57	*3	6	*3	*3	*3	*3	*3	*3	*3	*3	*3	*3	*3	3	6	0	3	0	3	Y	TOMO
127	9753949	200	57	*3	6	*3	*3	*3	*3	*3	*3	*3	*3	*3	*3	*3	3	6	0	3	0	3	Y	TOMO
128	9755013	200	43	1	6	0	0	0	0	*3	*3	*3	*3	*3	*3	*3	3	6	0	3	0	3	Y	TOMO
129	9941081	200	57	*3	6	*3	*3	*3	*3	*3	*3	*3	*3	*3	*3	*3	3	6	0	3	0	3	Y	TOMO
130	14000376	200	3	1	0	0	0	0	0	0	0	0	0	0	0	0	0	0	0	1	0	1	Y	EXTRA
131	14077668	300	60	*3	6	*3	*3	*3	*3	*3	*3	*3	*3	*3	*3	*3	*3	6	3	3	0	3	Y	TOMO
132	9038699	120	3	1	0	0	0	0	0	0	0	0	0	0	0	0	0	0	0	1	0	1	Y	EXTRA
133	9064568	120	3	1	0	0	0	0	0	0	0	0	0	0	0	0	0	0	0	1	0	1	Y	EXTRA
134	9093975	200	3	1	0	0	0	0	0	0	0	0	0	0	0	0	0	0	0	1	0	1	Y	EXTRA
135	9644101	120	58	*3	6	*3	*3	*3	*3	*3	*3	*3	*3	*3	*3	*3	*3	6	*3	1	0	3	Y	TOMO
136	9703873	200	61	*3	6	*3	*3	*3	*3	*3	*3	*3	*3	*3	*3	*3	*3	6	*3	3	1	3	Y	TOMO
137	9716853	120	60	*3	6	*3	*3	*3	*3	*3	*3	*3	*3	*3	*3	*3	*3	6	*3	3	0	3	Y	TOMO
138	9735129	120	41	*3	6	*3	*3	*3	*3	1	0	1	0	0	0	0	*3	6	*3	3	0	3	Y	TOMO
139	9818433	200	61	*3	6	*3	*3	*3	*3	*3	*3	*3	*3	*3	*3	*3	*3	6	*3	3	1	3	Y	TOMO
140	10094253	120	10	1	0	0	0	0	0	1	0	0	0	0	0	0	0	6	0	1	0	1	Y	EXTRA
141	14383980	300	16	1	6	0	0	0	0	0	0	1	1	1	1	1	1	0	0	1	1	1	N	EXTRA
142	3298292	120	3	1	0	0	0	0	0	0	0	0	0	0	0	0	0	0	0	1	0	1	Y	EXTRA
143	9064093	120	3	1	0	0	0	0	0	0	0	0	0	0	0	0	0	0	0	1	0	1	Y	EXTRA
144	7112721	120	3	1	0	0	0	0	0	0	0	0	0	0	0	0	0	0	0	1	0	1	Y	EXTRA

145	9069997	120	3	1	0	0	0	0	0	0	0	0	0	0	0	0	0	0	0	1	0	1	Y	EXTRA
146	9070083	120	3	1	0	0	0	0	0	0	0	0	0	0	0	0	0	0	0	1	0	1	Y	EXTRA
147	9105672	120	43	*3	6	*3	*3	*3	*3	3	0	1	0	0	0	0	*3	6	*3	3	0	3	Y	TOMO
148	9128775	200	41	*3	6	*3	*3	*3	*3	3	0	1	0	0	0	0	*3	6	1	3	0	3	Y	TOMO
149	9132433	120	4	1	0	0	0	0	0	1	0	0	0	0	0	0	0	0	0	1	0	1	Y	EXTRA
150	9140050	120	60	*3	6	*3	*3	*3	*3	*3	*3	*3	*3	*3	*3	*3	*3	6	*3	3	0	3	Y	TOMO
151	9169867	120	41	*3	6	*3	*3	*3	*3	1	0	1	0	0	0	0	*3	6	*3	3	0	3	Y	TOMO
152	9627721	200	43	*3	6	*3	*3	*3	*3	3	0	1	0	0	0	0	*3	6	*3	3	0	3	Y	TOMO
153	9627953	120	3	1	0	0	0	0	0	0	0	0	0	0	0	0	0	0	0	1	0	1	Y	EXTRA
154	9652545	120	3	1	0	0	0	0	0	0	0	0	0	0	0	0	0	0	0	1	0	1	Y	EXTRA
155	9655209	120	43	*3	6	*3	*3	*3	*3	3	0	1	0	0	0	0	*3	6	*3	3	0	3	Y	TOMO
156	9666905	120	43	*3	6	*3	*3	*3	*3	3	0	1	0	0	0	0	*3	6	*3	3	0	3	Y	TOMO
157	10972299	120	60	*3	6	*3	*3	*3	*3	*3	*3	*3	*3	*3	*3	*3	*3	6	*3	3	0	3	Y	TOMO
158	9734033	120	37	*3	6	*3	*3	*3	*3	1	0	1	0	0	0	0	*3	6	1	1	0	3	Y	TOMO
159	13692644	120	41	*3	6	*3	*3	*3	*3	1	0	1	0	0	0	0	*3	6	*3	3	0	3	Y	TOMO
160	13935988	300	43	*3	6	*3	*3	*3	*3	3	0	1	0	0	0	0	*3	6	*3	3	0	3	Y	TOMO
161	13936432	120	43	*3	6	*3	*3	*3	*3	3	0	1	0	0	0	0	*3	6	*3	3	0	3	Y	TOMO
162	13936596	120	3	1	0	0	0	0	0	0	0	0	0	0	0	0	0	0	0	1	0	1	Y	EXTRA
163	13936812	200	43	*3	6	*3	*3	*3	*3	3	0	1	0	0	0	0	*3	6	*3	3	0	3	Y	TOMO
164	13938812	200	43	*3	6	*3	*3	*3	*3	3	0	1	0	0	0	0	*3	6	*3	3	0	3	Y	TOMO
165	13939856	120	3	1	0	0	0	0	0	0	0	0	0	0	0	0	0	0	0	1	0	1	Y	EXTRA
166	14079184	200	60	*3	6	*3	*3	*3	*3	*3	*3	*3	*3	*3	*3	*3	*3	6	*3	3	0	3	Y	TOMO
167	10059745	120	43	*3	6	*3	*3	*3	*3	3	0	1	0	0	0	0	*3	6	*3	3	0	3	Y	TOMO
168	14116920	120	41	*3	6	*3	*3	*3	*3	1	0	1	0	0	0	0	*3	6	*3	3	0	3	Y	TOMO
169	14116972	200	60	*3	6	*3	*3	*3	*3	*3	*3	*3	*3	*3	*3	*3	*3	6	*3	3	0	3	Y	TOMO
170	14155260	300	43	*3	6	*3	*3	*3	*3	3	0	1	0	0	0	0	*3	6	*3	3	0	3	Y	TOMO
171	14158696	120	41	*3	6	*3	*3	*3	*3	1	0	1	0	0	0	0	*3	6	*3	3	0	3	Y	TOMO
172	10148369	120	39	*3	6	*3	*3	*3	*3	1	0	1	0	0	0	0	*3	6	*3	1	0	3	Y	TOMO
173	10148421	200	43	*3	6	*3	*3	*3	*3	3	0	1	0	0	0	0	*3	6	*3	3	0	3	Y	TOMO
174	10187953	120	43	*3	6	*3	*3	*3	*3	3	0	1	0	0	0	0	*3	6	*3	3	0	3	Y	TOMO
175	14239184	200	43	*3	6	*3	*3	*3	*3	3	0	1	0	0	0	0	*3	6	*3	3	0	3	Y	TOMO
176	10370141	300	3	1	0	0	0	0	0	0	0	0	0	0	0	0	0	0	0	1	0	1	N	EXTRA
177	9085734	120	3	1	0	0	0	0	0	0	0	0	0	0	0	0	0	0	0	1	0	1	Y	EXTRA
178	9086693	120	3	1	0	0	0	0	0	0	0	0	0	0	0	0	0	0	0	1	0	1	Y	EXTRA
179	3317364	120	3	1	0	0	0	0	0	0	0	0	0	0	0	0	0	0	0	1	0	1	Y	EXTRA
180	9096656	120	3	1	0	0	0	0	0	0	0	0	0	0	0	0	0	0	0	1	0	1	Y	EXTRA
181	9627557	120	26	*3	0	*3	*3	*3	*3	1	0	0	0	0	0	0	0	6	0	1	0	3	Y	TOMO
182	9700049	120	26	*3	0	*3	*3	*3	*3	1	0	0	0	0	0	0	0	6	0	1	0	3	Y	TOMO
183	9718013	200	43	*3	6	*3	*3	*3	*3	3	0	1	0	0	0	0	*3	6	*3	3	0	3	Y	TOMO
184	9742277	120	43	*3	6	*3	*3	*3	*3	3	0	1	0	0	0	0	*3	6	*3	3	0	3	Y	TOMO
185	9774569	200	43	*3	6	*3	*3	*3	*3	3	0	1	0	0	0	0	*3	6	*3	3	0	3	Y	TOMO
186	13813696	120	3	1	0	0	0	0	0	0	0	0	0	0	0	0	0	0	0	1	0	1	Y	EXTRA
187	9853417	120	12	1	6	0	0	0	0	1	0	1	0	0	0	0	1	0	0	1	0	1	Y	EXTRA
188	9915709	120	3	1	0	0	0	0	0	0	0	0	0	0	0	0	0	0	0	1	0	1	Y	EXTRA
189	14073800	200	43	*3	6	*3	*3	*3	*3	3	0	1	0	0	0	0	*3	6	*3	3	0	3	Y	TOMO
190	14118096	200	43	*3	6	*3	*3	*3	*3	3	0	1	0	0	0	0	*3	6	*3	3	0	3	Y	TOMO
191	14151344	300	43	*3	6	*3	*3	*3	*3	3	0	1	0	0	0	0	*3	6	*3	3	0	3	Y	TOMO
192	10223765	200	41	*3	6	*3	*3	*3	*3	3	0	1	0	0	0	0	*3	6	*3	1	0	3	Y	TOMO
193	9826789	200	43	*3	6	*3	*3	*3	*3	3	0	1	0	0	0	0	*3	6	*3	3	0	3	Y	TOMO
194	14133048	200	34	*3	6	*3	*3	*3	*3	1	0	1	0	0	0	0	1	6	0	1	0	3	Y	TOMO
195	14183744	120	41	*3	6	*3	*3	*3	*3	1	0	1	0	0	0	0	*3	6	*3	3	0	3	Y	TOMO
196	14236768	300	43	*3	6	*3	*3	*3	*3	3	0	1	0	0	0	0	*3	6	*3	3	0	3	Y	TOMO
197	14255632	120	41	*3	6	*3	*3	*3	*3	1	0	1	0	0	0	0	*3	6	*3	3	0	3	Y	TOMO
198	10230869	200	24	1	6	0	0	0	0	3	0	1	0	0	0	0	3	6	0	3	0	1	Y	EXTRA
199	9148510	200	3	1	0	0	0	0	0	0	0	0	0	0	0	0	0	0	0	1	0	1	Y	EXTRA
200	9150059	200	3	1	0	0	0	0	0	0	0	0	0	0	0	0	0	0	0	1	0	1	Y	EXTRA
201	9152745	120	3	1	0	0	0	0	0	0	0	0	0	0	0	0	0	0	0	1	0	1	Y	EXTRA
202	9154092	300	43	*3	6	*3	*3	*3	*3	3	0	1	0	0	0	0	*3	6	*3	3	0	3	Y	TOMO
203	9154179	200	3	1	0	0	0	0	0	0	0	0	0	0	0	0	0	0	0	1	0	1	Y	EXTRA
204	9154233	200	10	1	0	0	0	0	0	1	0	0	0	0	0	0	0	6	0	1	0	1	Y	EXTRA
205	9722529	200	18	1	6	0	0	0	0	1	0	1	0	0	0	0	1	6	0	1	0	1	Y	EXTRA

206	9722633	200	40	*3	6	*3	*3	*3	*3	3	0	1	0	0	0	0	3	6	0	3	0	3	Y	TOMO
207	9817605	200	3	1	0	0	0	0	0	0	0	0	0	0	0	0	0	0	0	1	0	1	Y	EXTRA
208	13966396	200	43	*3	6	*3	*3	*3	*3	3	0	1	0	0	0	0	*3	6	*3	3	0	3	Y	TOMO
209	13966672	200	10	1	0	0	0	0	0	1	0	0	0	0	0	0	0	6	0	1	0	1	Y	EXTRA
210	13970876	200	29	1	6	0	0	0	0	3	0	1	0	0	0	0	*3	6	*3	3	0	3	Y	TOMO
211	14178184	200	43	*3	6	*3	*3	*3	*3	3	0	1	0	0	0	0	*3	6	*3	3	0	3	Y	TOMO
212	14178188	200	43	*3	6	*3	*3	*3	*3	3	0	1	0	0	0	0	*3	6	*3	3	0	3	Y	TOMO
213	14178212	300	43	*3	6	*3	*3	*3	*3	3	0	1	0	0	0	0	*3	6	*3	3	0	3	Y	TOMO
214	14178236	300	38	*3	6	*3	1	0	*3	3	0	1	0	0	0	0	*3	6	*3	3	0	3	Y	TOMO
215	14178248	300	43	*3	6	*3	*3	*3	*3	3	0	1	0	0	0	0	*3	6	*3	3	0	3	Y	TOMO
216	14179288	120	22	1	6	0	0	0	0	3	0	1	0	0	0	0	1	6	0	3	0	1	Y	EXTRA
217	14179292	300	29	1	6	0	0	0	0	3	0	1	0	0	0	0	*3	6	*3	3	0	3	Y	TOMO
218	14179736	300	43	*3	6	*3	*3	*3	*3	3	0	1	0	0	0	0	*3	6	*3	3	0	3	Y	TOMO
219	9075784	120	3	1	0	0	0	0	0	0	0	0	0	0	0	0	0	0	0	1	0	1	Y	EXTRA
220	9075803	200	3	1	0	0	0	0	0	0	0	0	0	0	0	0	0	0	0	1	0	1	Y	EXTRA
221	12456160	120	34	*3	6	*3	*3	*3	*3	1	0	1	0	0	0	0	1	6	0	1	0	3	Y	TOMO
222	14072464	200	27	1	6	0	0	0	0	1	0	1	0	0	0	0	*3	6	*3	3	0	3	Y	TOMO
223	10186185	200	41	*3	6	*3	*3	*3	*3	1	0	1	0	0	0	0	*3	6	*3	3	0	3	Y	TOMO
224	10207681	200	38	*3	6	*3	*3	*3	*3	3	0	1	0	0	0	0	3	6	0	1	0	3	Y	TOMO
225	10215753	300	40	*3	6	*3	*3	*3	*3	3	0	1	0	0	0	0	3	6	0	3	0	3	Y	TOMO
226	14263544	200	43	*3	6	*3	*3	*3	*3	3	0	1	0	0	0	0	*3	6	*3	3	0	3	Y	TOMO
227	14263712	120	43	*3	6	*3	*3	*3	*3	3	0	1	0	0	0	0	*3	6	*3	3	0	3	Y	TOMO
228	14263768	200	40	*3	6	*3	*3	*3	*3	3	0	1	0	0	0	0	3	6	0	3	0	3	Y	TOMO
229	10226877	120	39	*3	6	*3	*3	*3	*3	1	0	1	0	0	0	0	*3	6	*3	1	0	3	Y	TOMO
230	9146641	300	43	*3	6	*3	*3	*3	*3	3	0	1	0	0	0	0	*3	6	*3	3	0	3	Y	TOMO
231	9660449	120	4	1	0	0	0	0	0	1	0	0	0	0	0	0	0	0	0	1	0	1	Y	EXTRA
232	9944301	200	29	1	6	0	0	0	0	3	0	1	0	0	0	0	*3	6	*3	3	0	3	Y	TOMO
233	14137160	120	34	*3	6	*3	*3	*3	*3	1	0	1	0	0	0	0	1	6	0	1	0	3	Y	TOMO
234	14181056	120	34	*3	6	*3	*3	*3	*3	1	0	1	0	0	0	0	1	6	0	1	0	3	Y	TOMO
			6794	502	852	400	395	389	389	370	123	222	121	109	103	97	390	954	264	479	115	520		

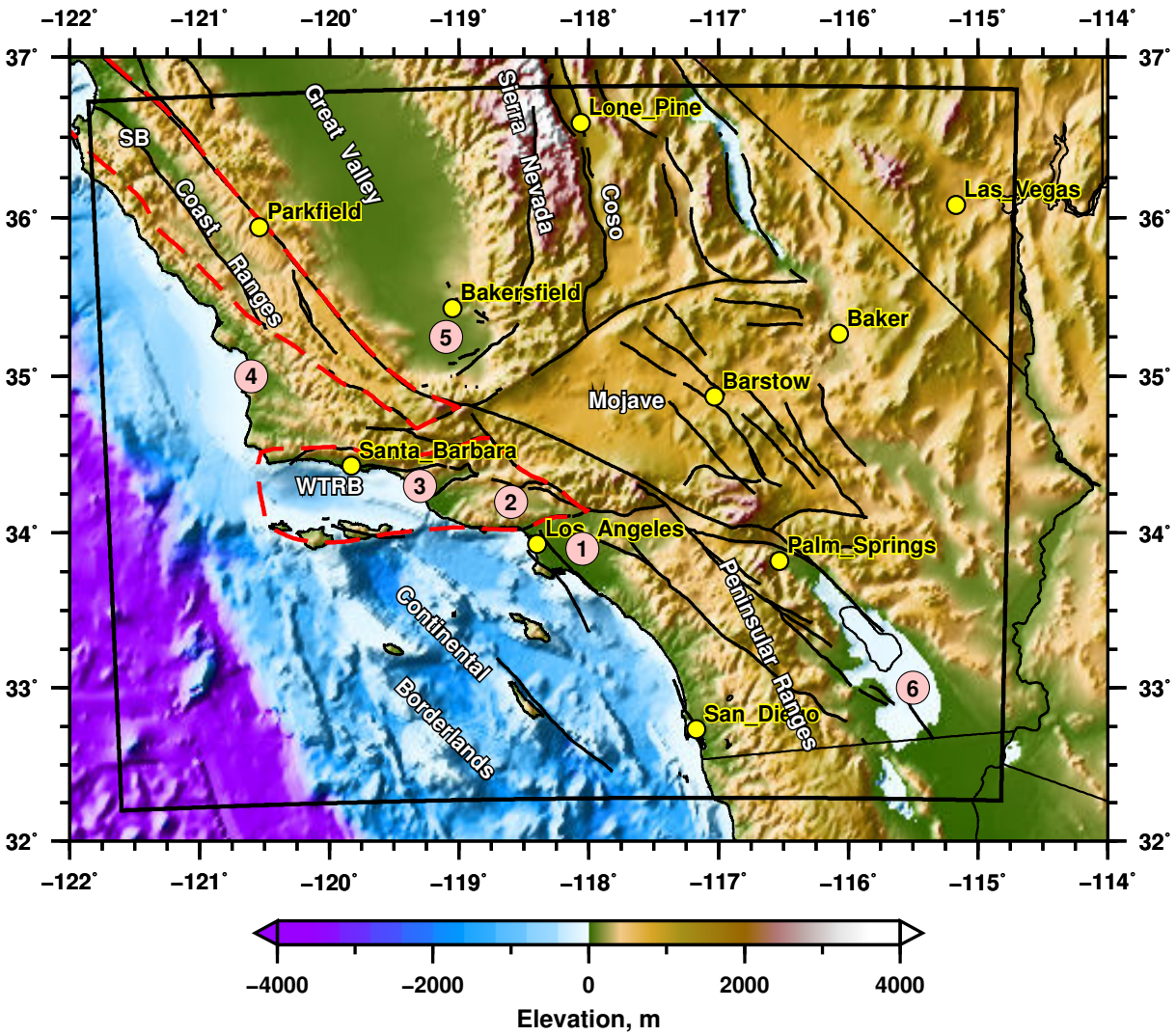

Figure 6.1: Base map for crustal tomography study of southern California. (a) Map shows topography and bathymetry (*Amante and Eakins*, 2008), as well as active faults (*Jennings*, 1994). Labels 1–6 denote the sedimentary basins of (1) Los Angeles, (2) San Fernando, (3) Ventura–Santa Barbara, (4) Santa Maria, (5) southern San Joaquin, and (6) the Salton trough, all of which have been active during the Neogene. Dashed red lines outline blocks that have undergone substantial Neogene motion: the Salinian block (SB) within the Coast Ranges, and the western Transverse Ranges block (WTRB). The black outline denotes the simulation region, which extends to 60 km depth. (b: next page) Selected principal faults in addition to nine segments denoting tomographic cross sections shown in other figures. Each cross section is an extended source-station path, with the earthquake epicenter at the star and the station at the triangle. Active faults are from *Jennings* (1994), plus the Kern Canyon fault (*Nadin and Saleeby*, 2009). Faults labeled for reference in each cross section figure are drawn in bold red and labeled in the boxes: SA, San Andreas, KC, Kern Canyon, SN, Sierra Nevada, G, Garlock, CR, Camp Rock, SG, San Gabriel, SY, Santa Ynez, MC, Malibu Coast, E, Elsinore. The Camp Rock fault, as labeled, includes a connection of faults from north to south: Gravel Hills–Harper fault, Harper Lake fault, Camp Rock fault, and Emerson fault. The Malibu Coast fault is drawn in continuation to the west to mark the southern boundary of the Western Transverse Ranges block (WTRB); the Santa Ynez fault is drawn in continuation to the west to mark the northern boundary of the WTRB (*Luyendyk et al.*, 1980).

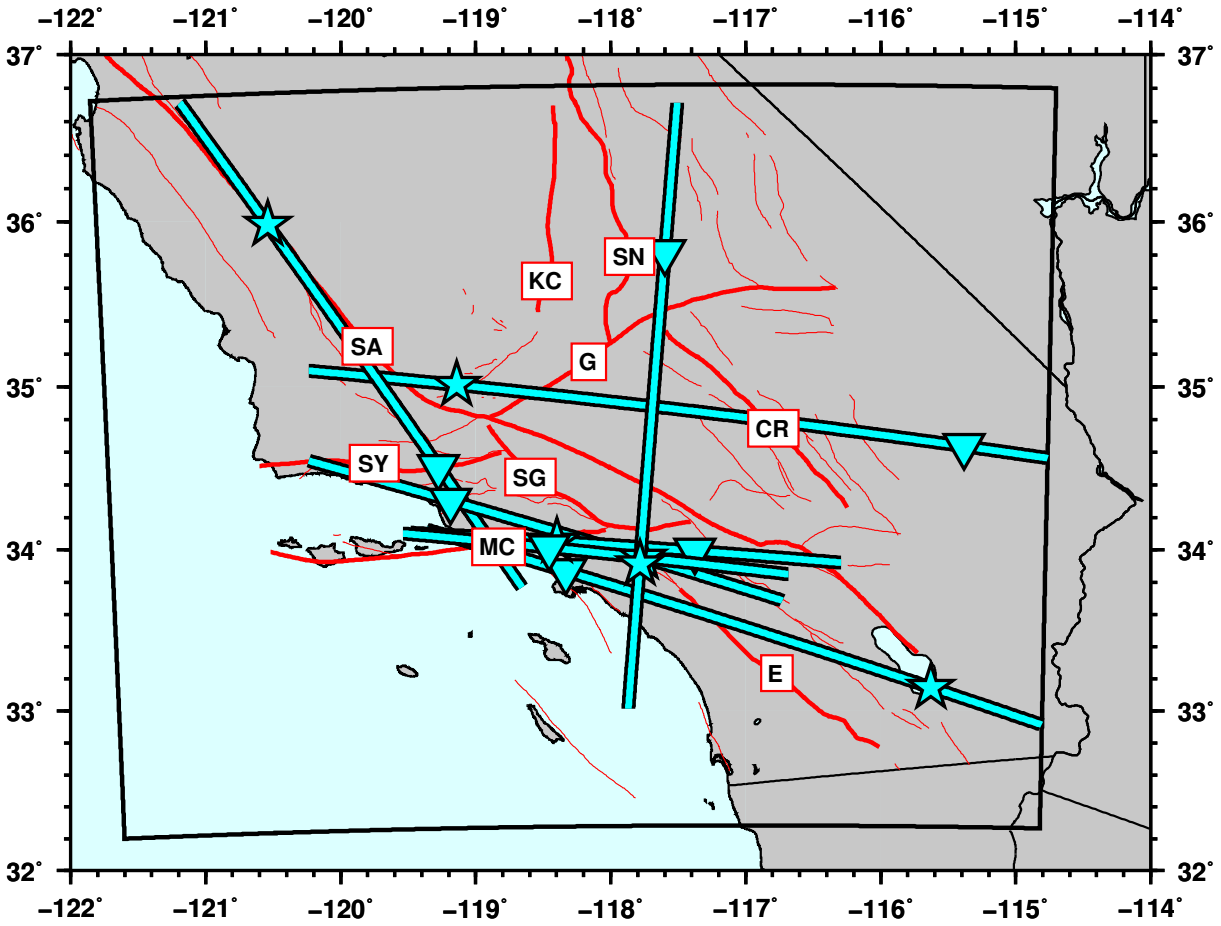
−122˚
−121˚
−120˚
−119˚
−118˚
−117˚
−116˚
−115˚
−114˚
37˚
36˚
35˚
34˚
33˚
32˚
SA
KC
SN
G
CR
SY
SG
MC
E

Figure 6.1b

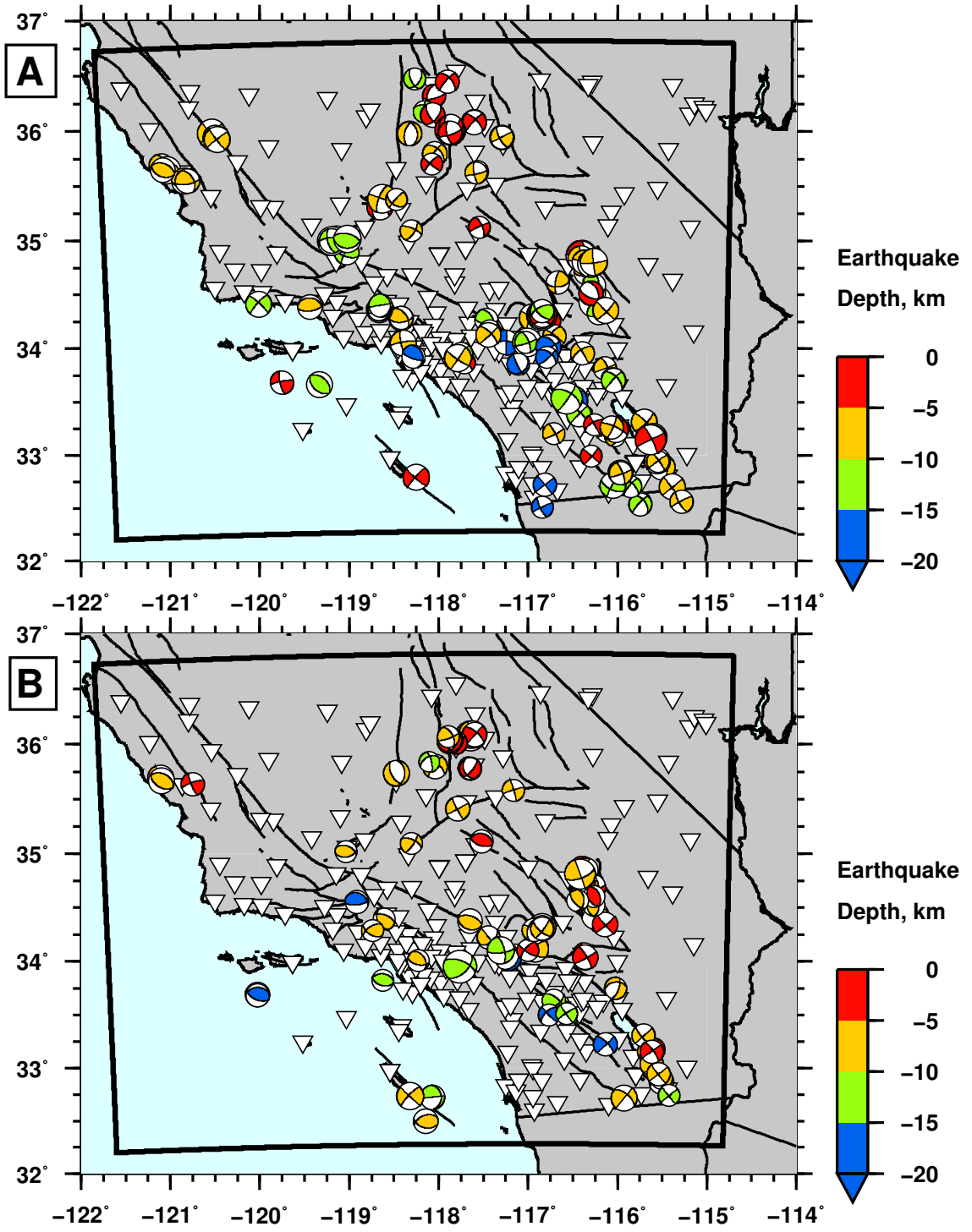

Figure 6.2: (a) Earthquake sources (143) and stations used in the tomographic inversion. Black boundary denotes our simulation region; blue boundary denotes the model of *Lin et al.* (2007b) used in the initial 3D model $\mathbf{m}_{00}$. (b) Extra earthquakes (91) used in validating the final tomographic model, but not used in the tomographic inversion. An earthquake not used in the tomographic inversion—or any future earthquake, for that matter—may be used to independently assess the misfit reduction from $\mathbf{m}_{00}$ to $\mathbf{m}_{16}$.

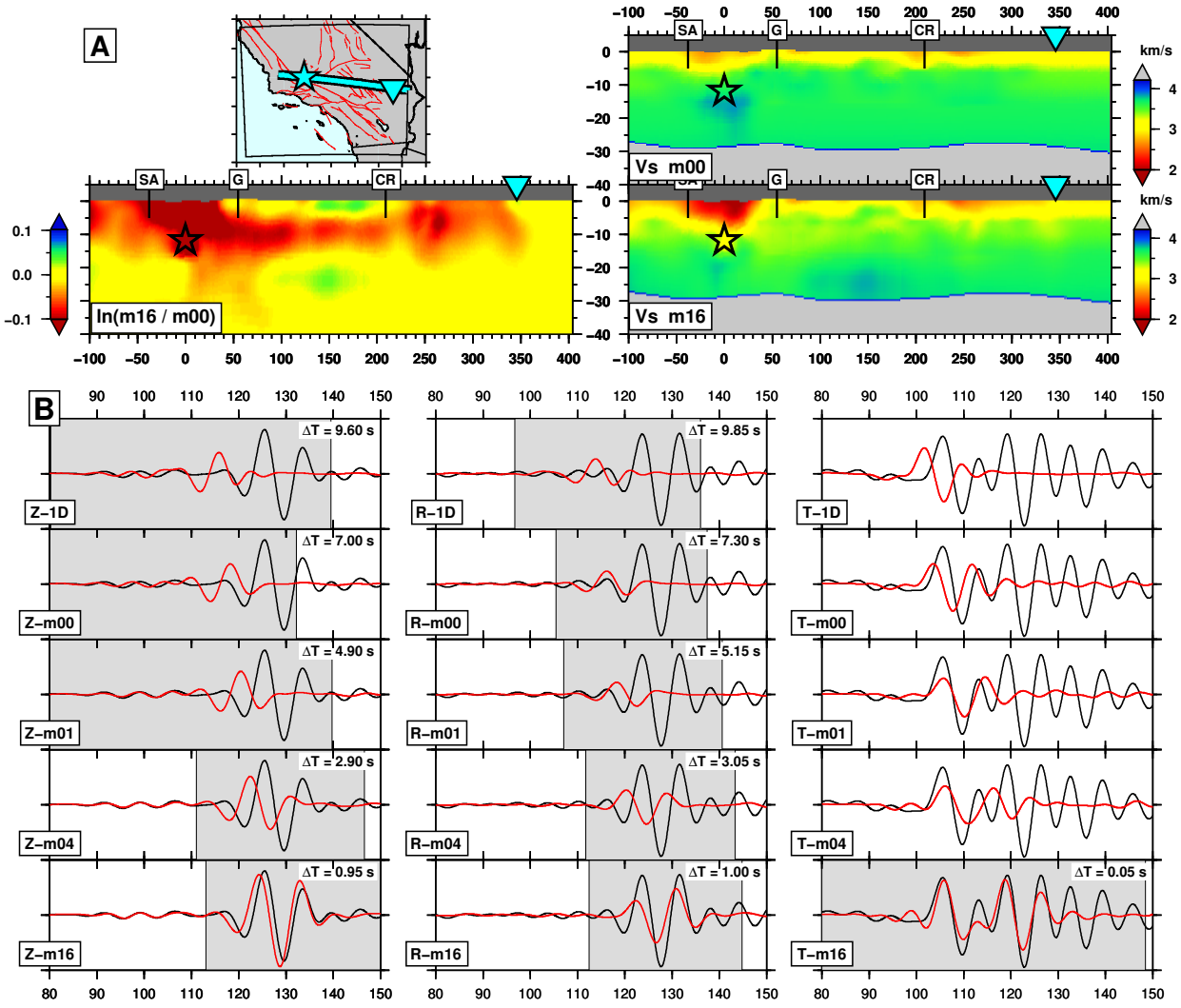

Figure 6.3: (a) Cross section of the V_S tomographic models for a path from a M_w 4.5 earthquake on the White Wolf fault (star label) to station DAN (triangle label) in the eastern Mojave Desert. Upper right is the initial 3D model, $\mathbf{m}_{00}$, lower right is the final 3D model, $\mathbf{m}_{16}$, and lower left is the difference between the two, $\ln(\mathbf{m}_{16}/\mathbf{m}_{00})$. Vertical exaggeration in these cross sections, and all cross sections in the paper, is 3.0. Boxed labels with vertical lines denote the position of various faults for reference: San Andreas (SA), Garlock (G), and Camp Rock (CR). (b) Iterative three-component seismogram fits to data for models $\mathbf{m}_{00}$, $\mathbf{m}_{01}$, $\mathbf{m}_{04}$, and $\mathbf{m}_{16}$. Also shown are synthetic seismograms computed for a standard 1D model (Table 6.1). Synthetic seismograms (red) and recorded seismograms (black), filtered over the period range 6–30 s. Left column, vertical component (Z); center column, radial component (R); right column, transverse component (T). Inset "ΔT" label indicates the time shift between the two windowed records *Maggi et al.* (2009) that provides the maximum cross-correlation.

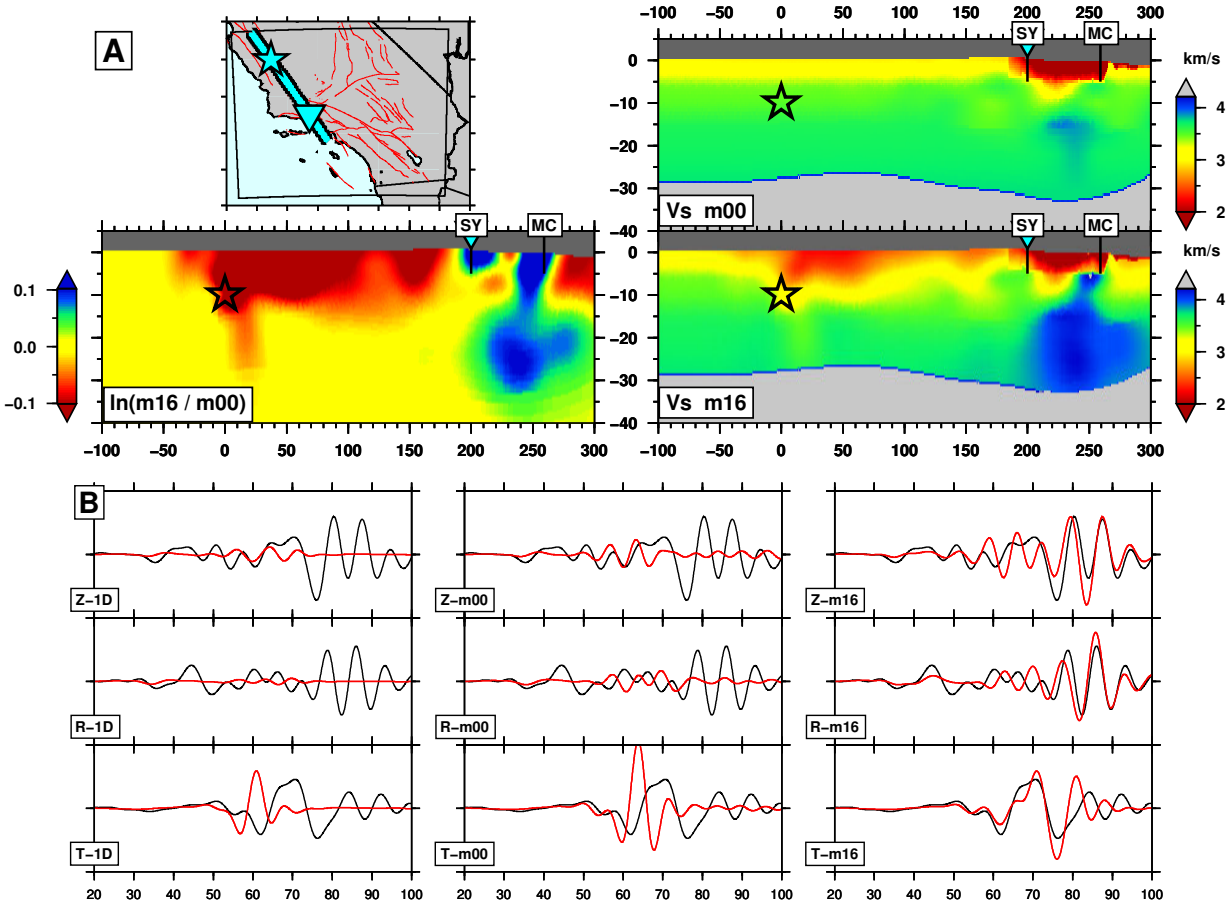

Figure 6.4: Cross sections of the tomographic model with corresponding seismograms. Measurement windows are omitted to emphasize the full waveforms. Boxed labels with vertical lines denote the location of the faults for reference: MC, Malibu Coast, SY, Santa Ynez. (a) Path for a M_w 4.6 earthquake near Parkfield to station WGR, just north of the Ventura basin. (b) Synthetic seismograms (red) and recorded seismograms (black) for the period range 6–30 s. (c: next page) Path for a M_w 5.4 earthquake near Chino Hills to station STC, within the Ventura basin. (d: next page) Corresponding seismograms.

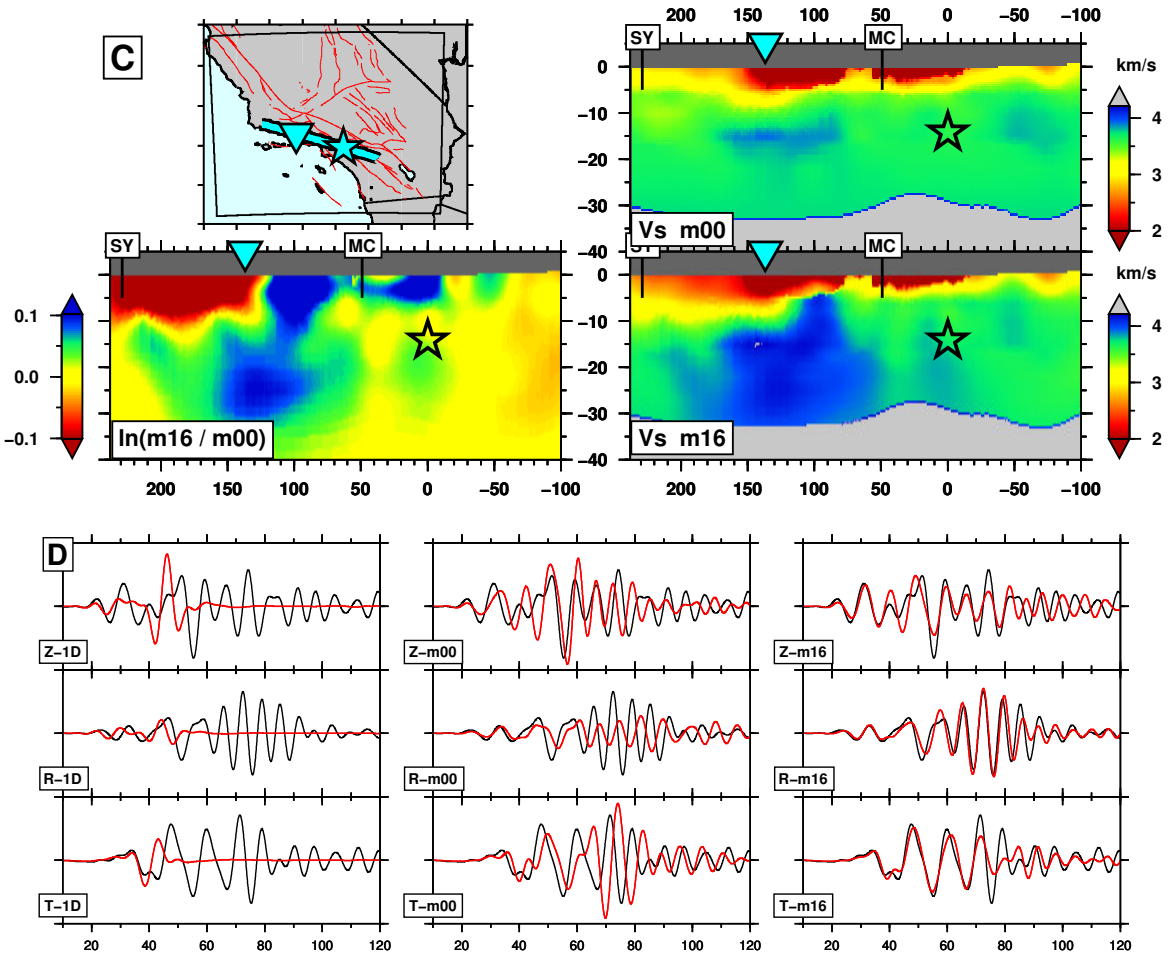
C
SY
MC
Vs m00
Vs m16
ln(m16 / m00)
km/s
D
Z–1D
R–1D
T–1D
Z–m00
R–m00
T–m00
Z–m16
R–m16
T–m16

Figure 6.4c–d

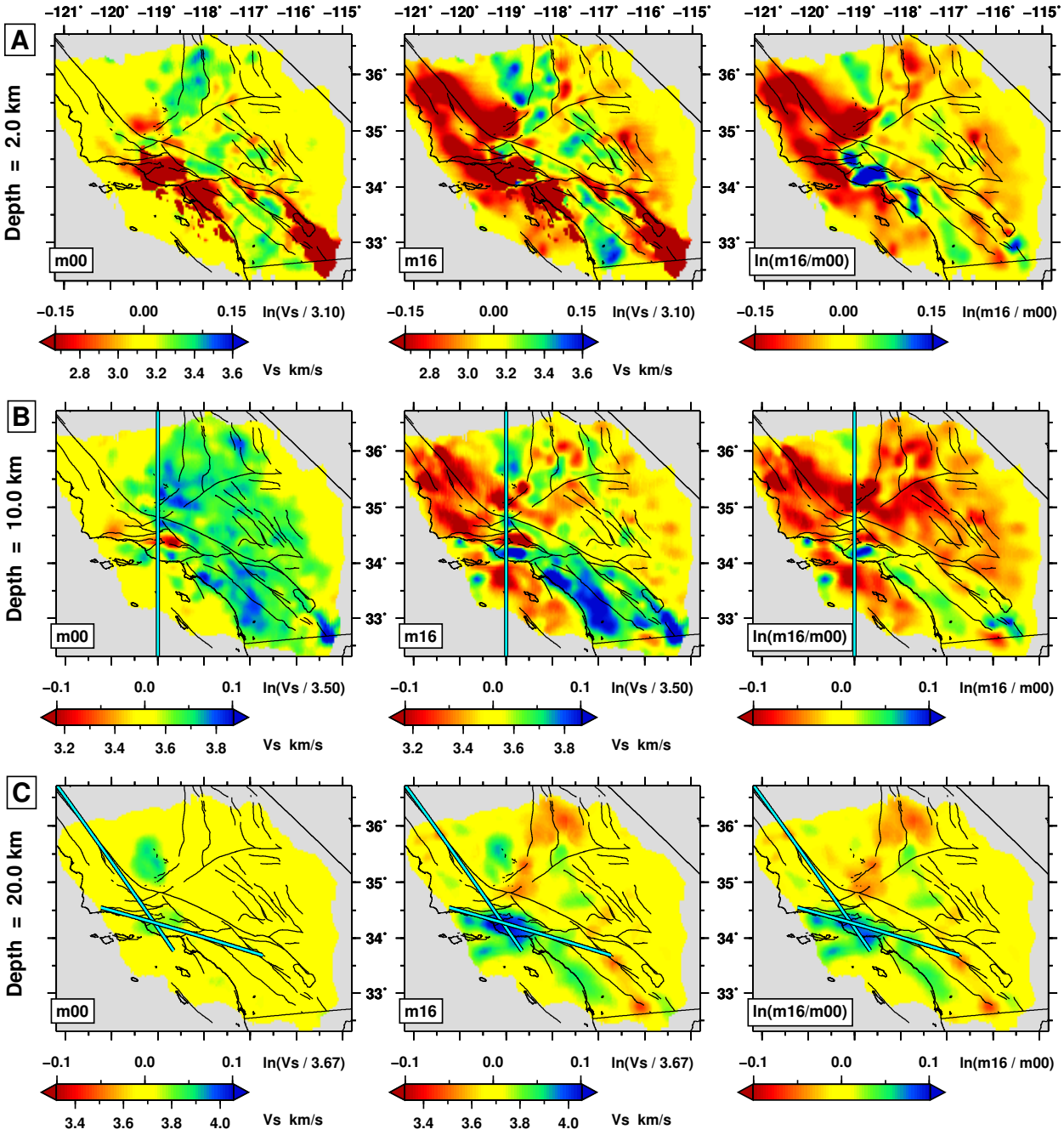

Figure 6.5: Horizontal cross sections of V_S tomographic models, with active faults shown for reference. Refer to Figure 6.1 for locations of principal faults and features. Left column shows the initial model, $\mathbf{m}_{00}$, center column shows the final model, $\mathbf{m}_{16}$, and right column shows the difference between the two models, $\ln(\mathbf{m}_{16}/\mathbf{m}_{00})$. The mask covers regions of low sensitivity to changes in V_S. (a) V_S at 2 km depth. (b) V_S at 10 km depth. The variation along longitude 119°W is discussed in the text. (c) V_S at 20 km. The two ray paths crossing the western Transverse Ranges block correspond to the profiles of Figure 6.4a, c.

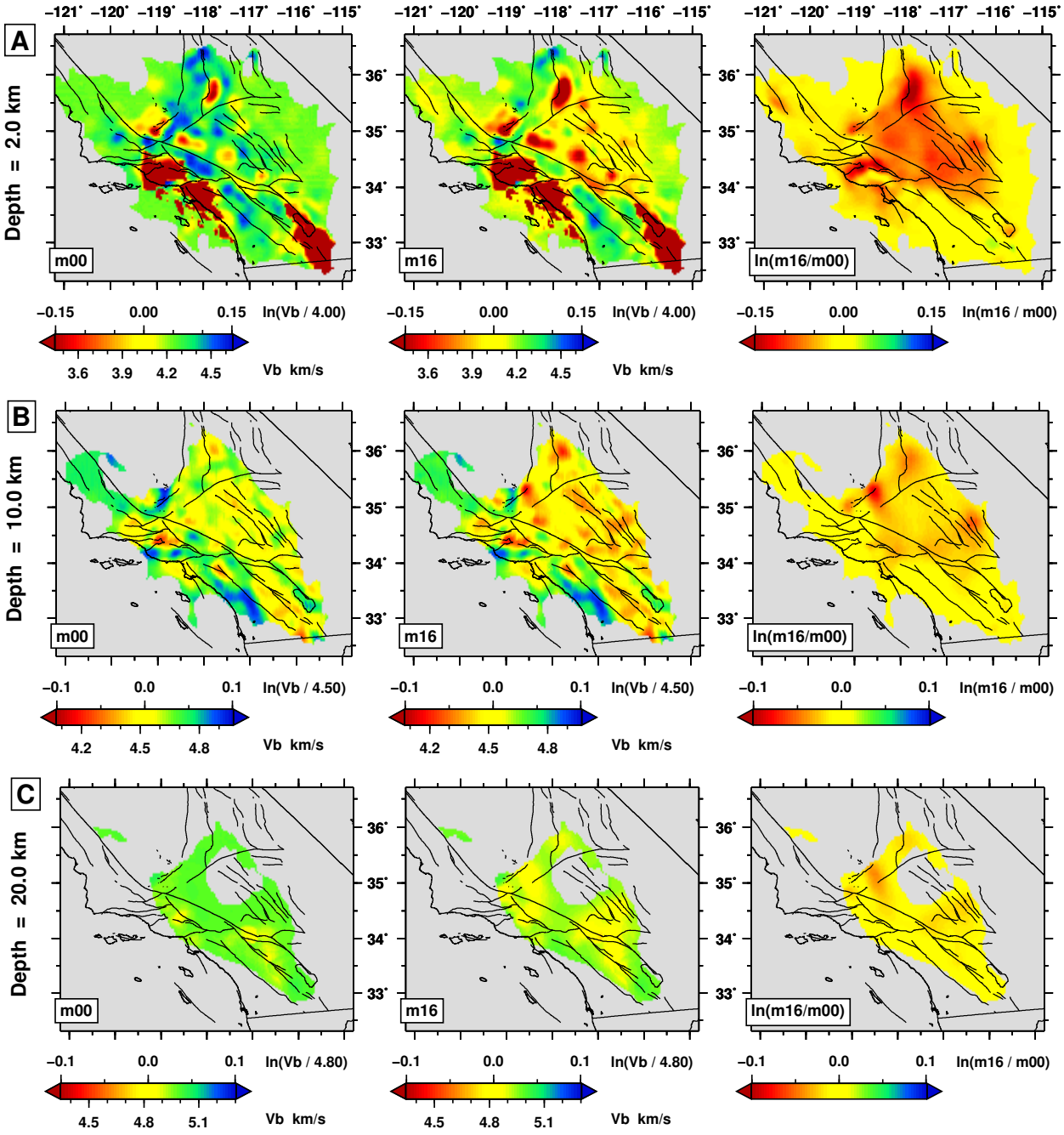

Figure 6.6: Horizontal cross sections of bulk-sound speed V_B tomographic models, with active faults shown for reference. Refer to Figure 6.1 for locations of principal faults and features. Left column shows the initial model, $\mathbf{m}_{00}$, center column shows the final model, $\mathbf{m}_{16}$, and right column shows the difference between the two models, $\ln(\mathbf{m}_{16}/\mathbf{m}_{00})$. The mask covers regions of low sensitivity to changes in V_B. (a) V_B at 2 km depth. (b) V_B at 10 km depth. (c) V_B at 20 km.

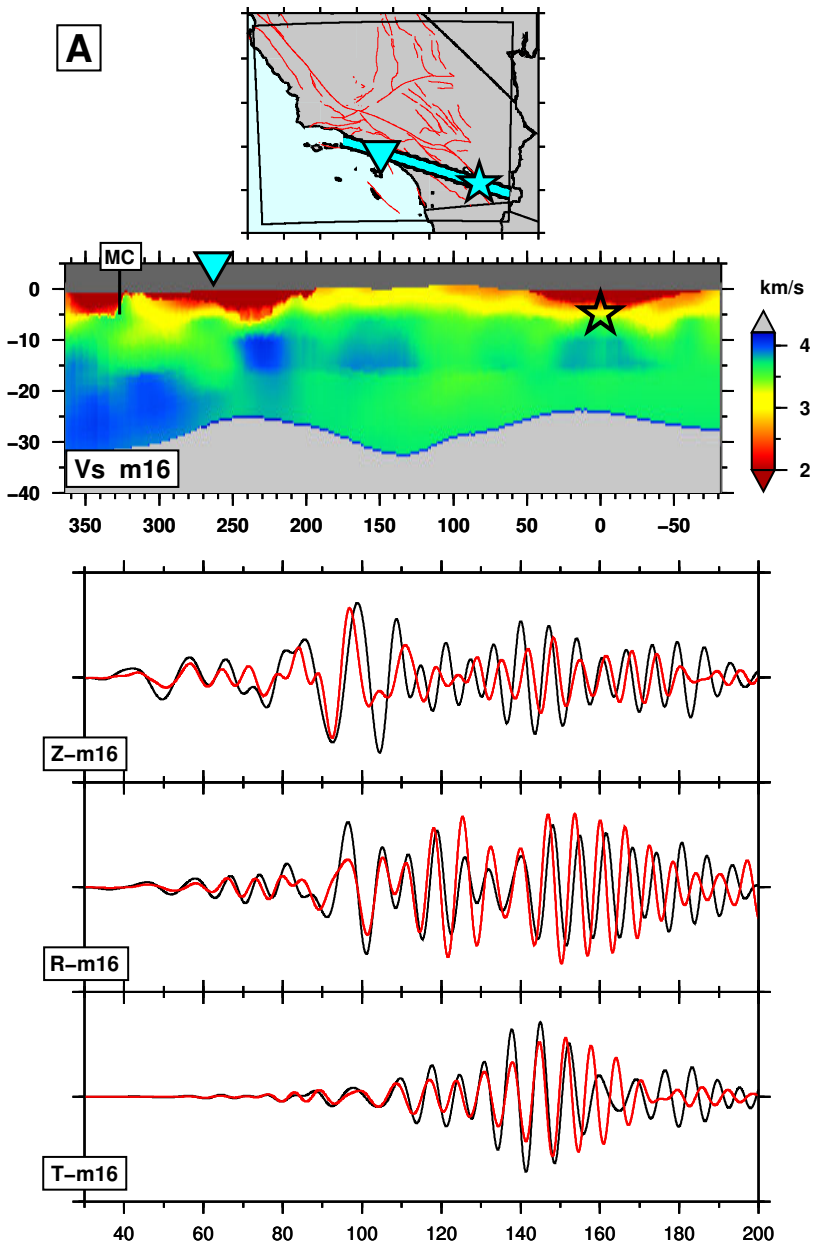

Figure 6.7: Seismogram fits between data (black) and synthetics (red) for selected paths in the final model. Each earthquake (star) is modeled as a point-source focal mechanism. Cross section shows the V_S model $\mathbf{m}_{16}$ between the source and station. Boxed labels with vertical lines denote the position of the faults for reference: SA, San Andreas, G, Garlock, SG, San Gabriel, MC, Malibu Coast. (a) Earthquake 14179736 (M_w 5.0) to station LAF.CI: period range 6–30 s, record length 170 s, source half duration 0.80 s. (b: following pages) Earthquake 9703873 (M_w 4.2) to station RVR.CI: period range 3–30 s, record length 70 s, source half duration 0.33 s. The gray time windows highlight three different Rayleigh wave arrivals whose approximate paths are marked in the adjacent inset map. The later two arrivals have interacted with the Los Angeles basin, south of the source, before reaching the station. (c: following pages) Earthquake 14383980 (M_w 5.4) to SMS.CI: period range 2–30 s, record length 50 s, source half duration 1.29 s. (d: following pages) Earthquake 9818433 (M_w 4.3) to CLC.CI: period range 2–30 s, record length 70 s, source half duration 0.39 s.

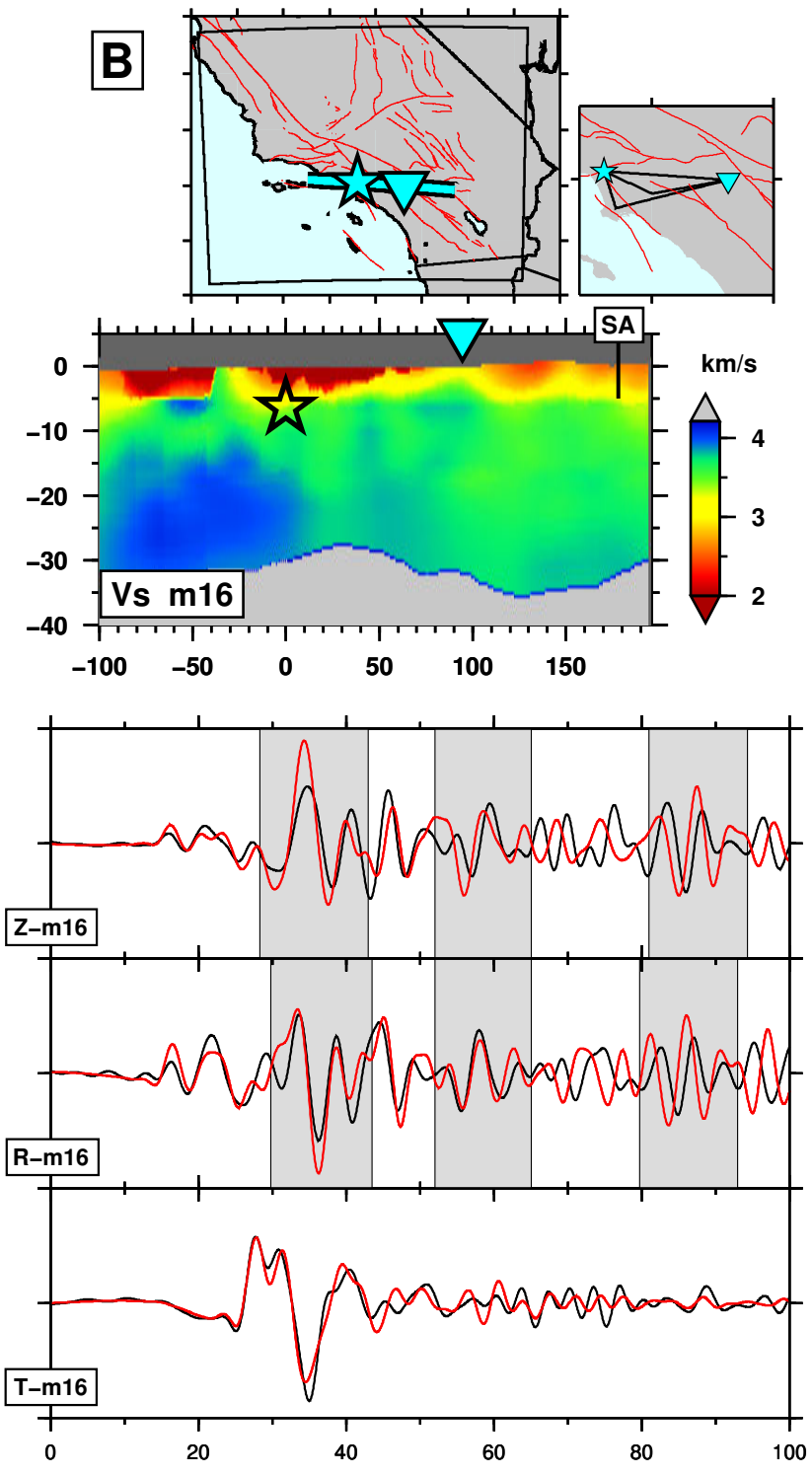
B
SA
km/s
4
3
2
0
−10
−20
−30
−40
Vs m16
−100
−50
0
50
100
150
Z−m16
R−m16
T−m16
0
20
40
60
80
100

Figure 6.7b

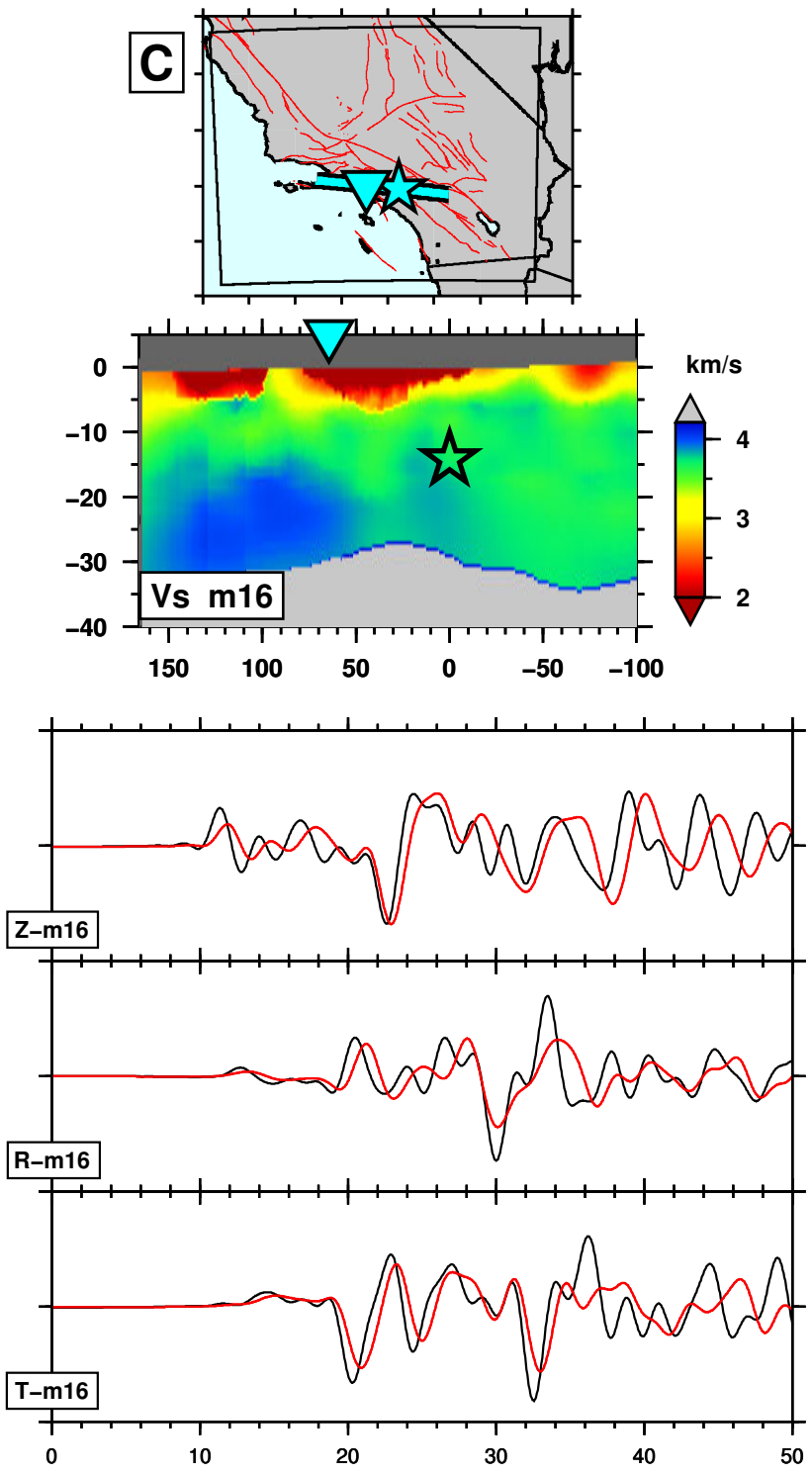
C
0
−10
−20
−30
−40
Vs m16
km/s
4
3
2
150
100
50
0
−50
−100
Z−m16
R−m16
T−m16
0
10
20
30
40
50

Figure 6.7c

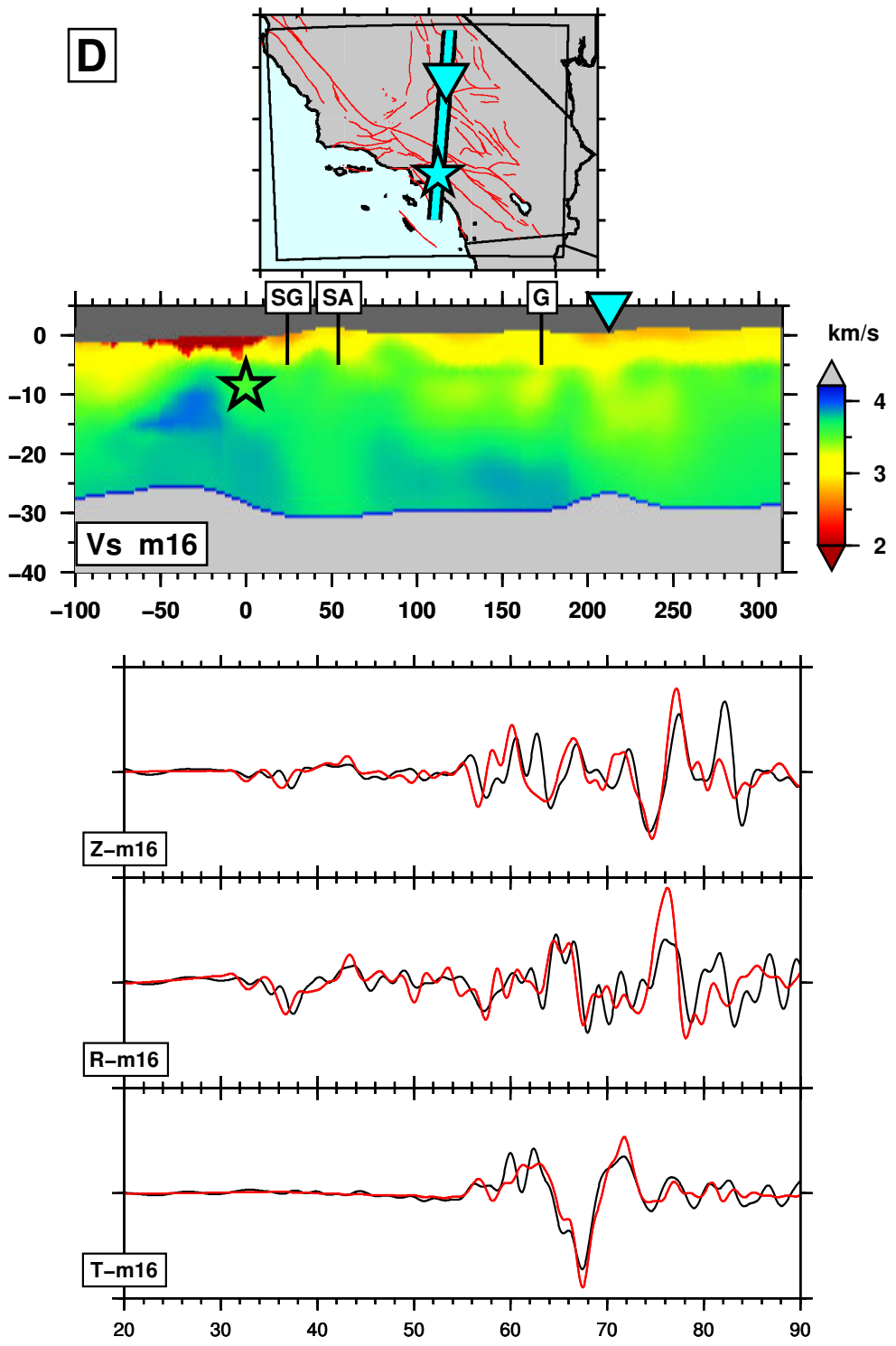
D
SG
SA
G
0
−10
−20
−30
−40
Vs m16
km/s
4
3
2
−100
−50
0
50
100
150
200
250
300
Z−m16
R−m16
T−m16
20
30
40
50
60
70
80
90

Figure 6.7d

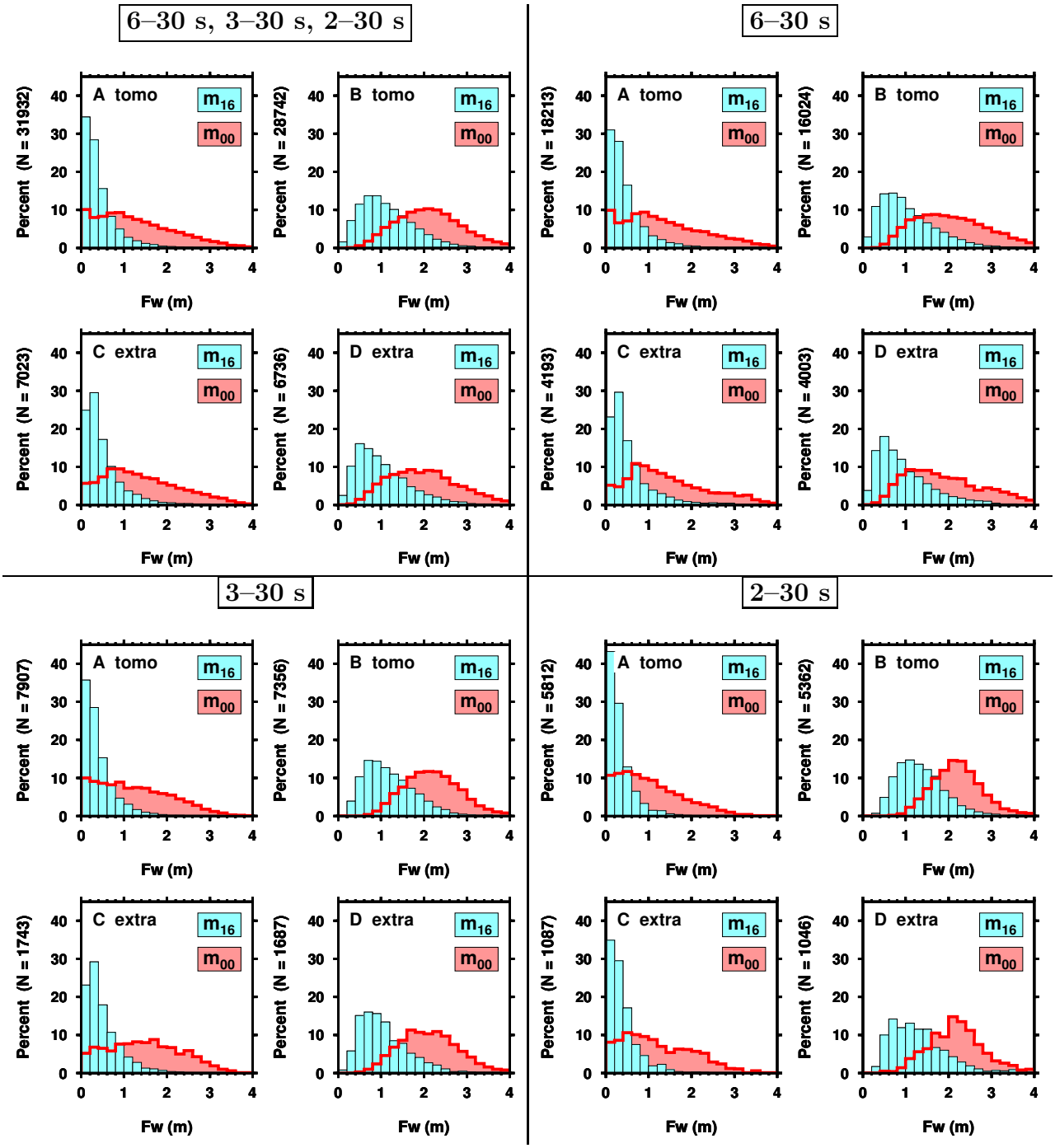

Figure 6.8: Waveform misfit analysis for the initial and final tomographic models, comparing 143 earthquakes used in the inversion (a, b: "tomo") with 91 additional earthquakes not used in the inversion (c, d: "extra"). There are four blocks of four subplots labeled (a)–(d). Each block corresponds to a different period range: all three period ranges (6–30 s, 3–30 s, and 2–30 s) (upper left), 6–30 s only (upper right), 3–30 s only (lower left), and 2–30 s only (lower right). (a) Waveform difference misfit values, $F_{\mathrm{w}}(\mathbf{m})$, for windows used in the inversion. $F_{\mathrm{w}}(\mathbf{m})$ is defined in Section 6.3. (b) Waveform difference misfit values for full seismograms containing a least one measurement window. (c)–(d) Same as (a)–(b), but for the set of extra earthquakes.

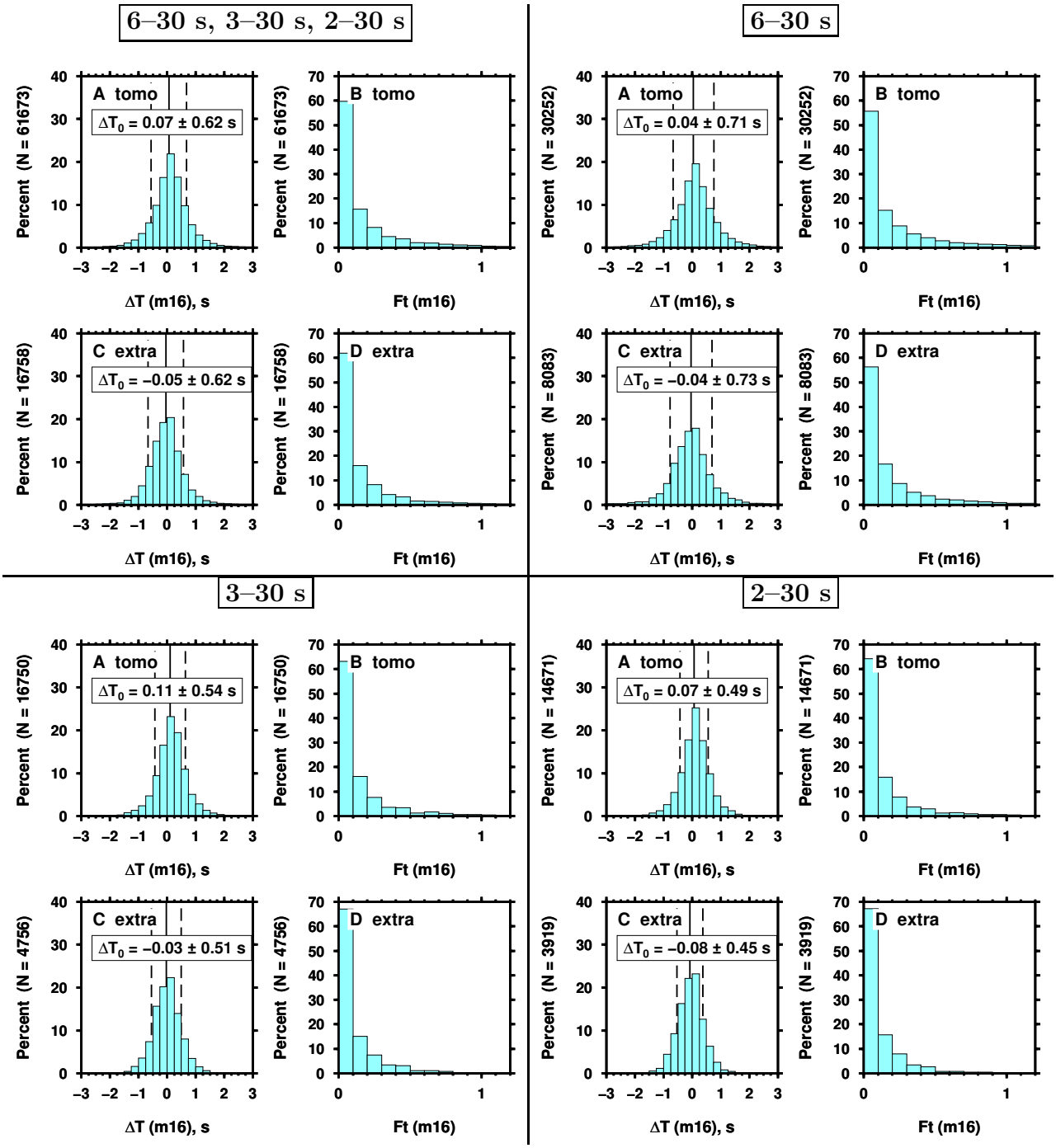

Figure 6.9: Traveltime differences within all seismogram windows used in the final tomographic model ($\mathbf{m}_{16}$) for different period ranges: all three period ranges (6–30 s, 3–30 s, and 2–30 s) (upper left), 6–30 s only (upper right), 3–30 s only (lower left), and 2–30 s only (lower right). In addition to the histogram of traveltime differences, $\Delta T(\mathbf{m}_{16})$, we also show the corresponding misfit measure, $F_{\mathrm{t}}(\mathbf{m}_{16})$.

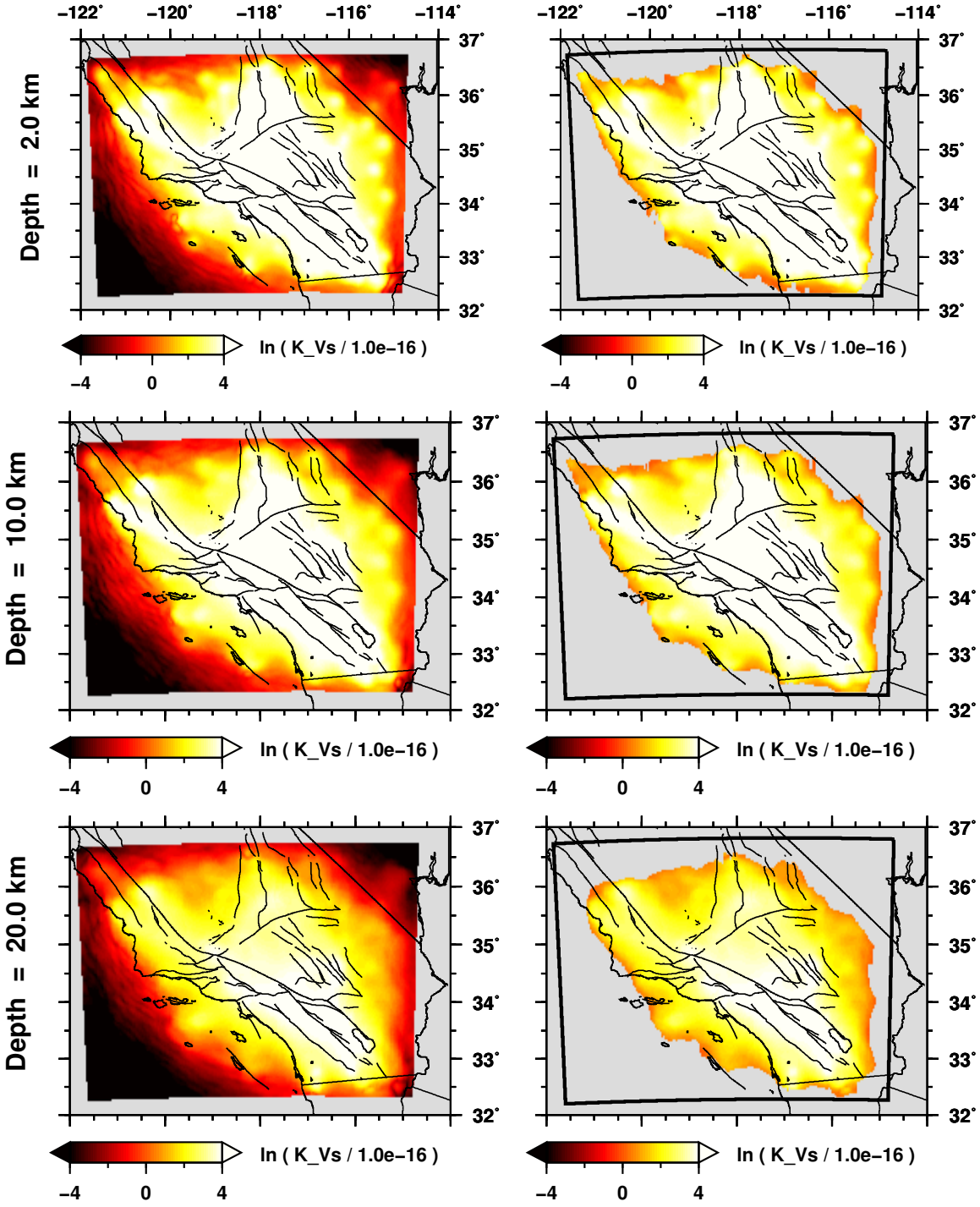

Figure 6.10: Volumetric coverage for the V_S tomographic model, plotted at three depths. The scalar field is computed as $\ln[K_{V_S}(\mathbf{x})/K_0]$, where $K_{V_S}(\mathbf{x})$ is the sum of all V_S kernels, and $K_0 = 10^{-16}$ m^{-3} is the threshold value that determines the mask shown in the right column. Note that the coverage diminishes with depth, because the short-period surface waves, which dominate the sensitivity, are more sensitive near the surface. The black outline denotes the simulation region, which extends to 60 km depth.

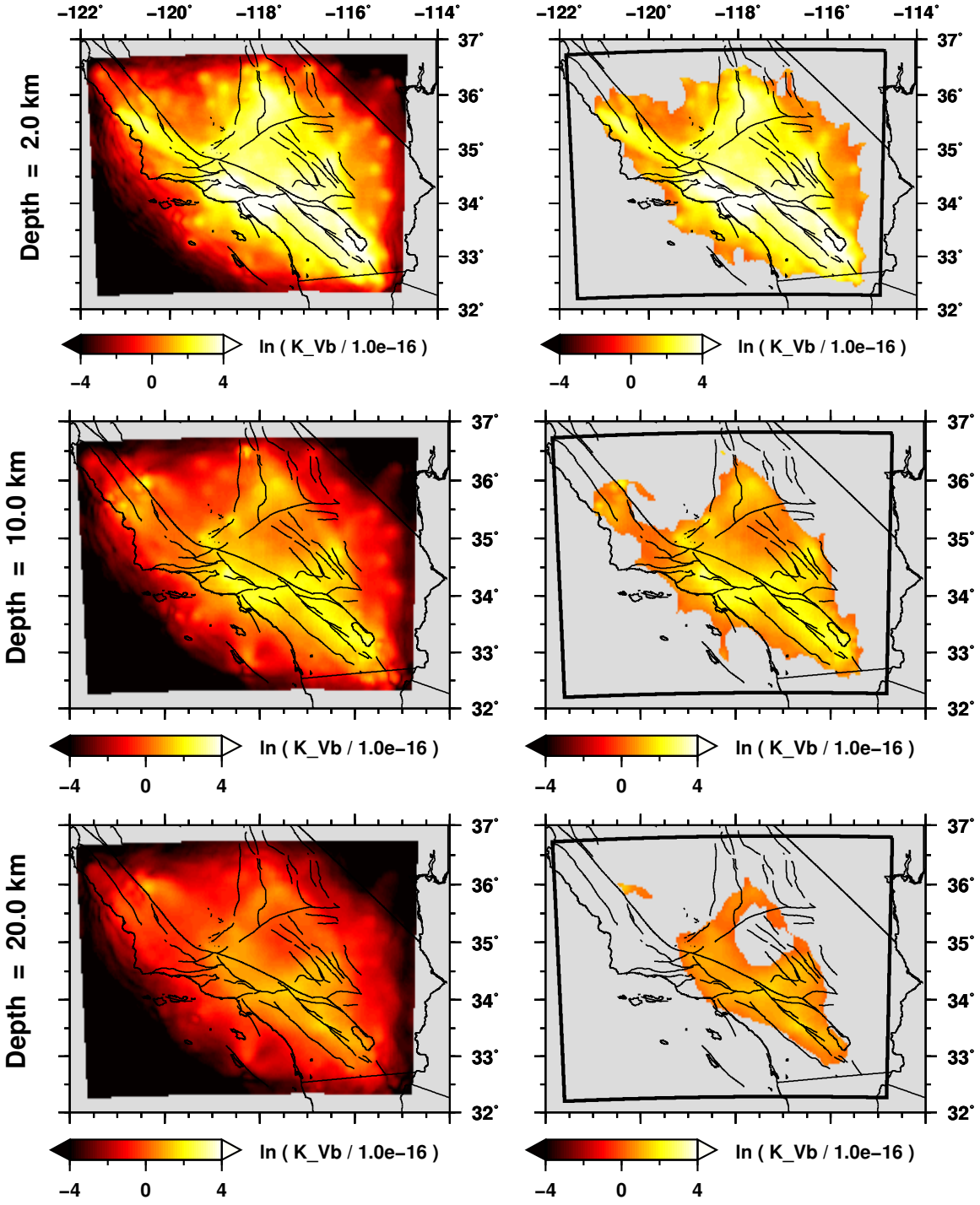

Figure 6.11: Volumetric coverage for the V_B tomographic model, plotted at three depths. The scalar field is computed as $\ln[K_{V_\mathrm{B}}(\mathbf{x})/K_0]$, where $K_{V_\mathrm{B}}(\mathbf{x})$ is the sum of all V_B kernels, and $K_0 = 10^{-16}$ m^{-3} is the threshold value that determines the mask shown in the right column.